

Damage development during flexural loading of a 5-directional braided C/C-SiC composite, characterized by X-ray tomography and digital volume correlation

Short title: Flexural damage in a braided composite

Fan Wan^{1, 2}, Rongjun Liu¹, Yanfei Wang¹, Yingbin Cao¹, Changrui Zhang¹ and Thomas James Marrow^{*2}

1. College of Aerospace Science and Technology, National University of Defense Technology, Changsha, 410073, China
2. Department of Materials, University of Oxford, Oxford, OX1 3PH, UK

*Corresponding Author:

Thomas James Marrow, james.marrow@materials.ox.ac.uk

Tel: 01865 273938, Fax: 01865 273289,

Email: james.marrow@materials.ox.ac.uk

Abstract

In situ observations of damage development within 3-dimensional 5-directional braided carbon fiber reinforced carbon and silicon carbide (C/C-SiC) ceramic composites, fabricated by gaseous silicon infiltration (GSI) and precursor infiltration pyrolysis (PIP), have been obtained using laboratory X-ray computed tomography during in situ flexural tests. The GSI composite has a denser structure than that fabricated by PIP, but contains initial defects within the fiber bundles. The GSI composite ultimately failed due to fracture across the fiber bundles, while failure of the higher strength PIP composite propagated along the interface between the fiber bundle and matrix with a greater degree of fiber pullout. These differences arise from the higher process temperature and greater degree of matrix-fiber reaction of GSI compared to PIP. Digital volume correlation (DVC), applied to the tomographs, measured the 3-dimensional deformations and hence the specimen curvature. This demonstrated the significant reduction in elastic modulus caused by the development of internal cracking with tensile strain in both materials.

Key Words

C/C-SiC; Flexural loading; Ceramic matrix composite; 3D braided; X-ray Computed Tomography; Digital Volume Correlation

1 Introduction

Carbon fiber reinforced carbon and silicon carbide composites (C/C-SiC) are important for aerospace structure components [1–3] because of their good high temperature mechanical properties and superior physical/chemical properties. They also find uses in advanced friction systems [4,5] due to their high coefficient of friction, high abrasion resistance and good maintenance of properties in wet environments, and are promising materials for applications in advanced nuclear energy [6] and ballistic protection [7]. For structural applications, there is a need to investigate and better understand the influence of both the fiber arrangement and the processing method on mechanical properties, as these affect how deformation and damage are accommodated. Fibers have anisotropic properties, and anisotropy in composites is generally controlled by using laminates or two-dimensional weaves. However, the through-thickness strength, stiffness, interlaminar shear strength, impact toughness and damage tolerance are low in such structures, and various concepts for reinforcement through the thickness direction have received attention in recent years, including the use of three dimensional (3D) textile patterns such as braiding, weaving and needling. Three-dimensional braided patterns are particularly interesting, and studies of 3D five-directional braiding in carbon fiber-resin systems have shown it allows the design of composites with more isotropic strength and stiffness [8,9] and excellent delamination resistance [10]. These properties rely on the mechanical interaction between the fibers and matrix [8], but are dominated by the fiber properties and architecture in polymer matrix composites. For ceramic composites, in which the stiffness of the matrix and fibers can be of similar magnitude, it is important to recognize that the internal strains, cracking and changes in the fiber-matrix interface that may be induced by processing are all important in determining the mechanical properties [11]. In the few studies of 3D five-directional braided ceramic matrix composites [12,13] that have been published, pre-existing defects have been identified as important factors.

There are many production methods for C/C-SiC composites, of which Precursor Infiltration and Pyrolysis (PIP) and Silicon infiltration (SI) are two of the most frequently used [4]. The PIP method [14–16] has a relative low reaction temperature that tends not to damage to the fibers. PIP-fabricated materials therefore usually have good mechanical properties, although large porosity (10~15%) can occur due to inadequate infiltration of the precursor and the escape of gases during pyrolysis. The SI method, which includes Liquid Silicon Infiltration (LSI) [17,18] and Gaseous Silicon Infiltration (GSI) [19,20], offers a shorter fabrication process than PIP and can produce compact structures with less than 5% porosity. However, the high reaction temperature of SI may cause damage to fibers [21] that together with the effects of residual silicon [4,22] can be detrimental to the mechanical properties.

Good mechanical properties are a basic requirement for C/C-SiC composites in load-bearing structures. Consequently, research has been conducted to investigate the mechanical behavior and damage mechanisms in C/C-SiC composites. For example, Weigel et al. [23] studied 2D C/C-SiC composites that were loaded by tension, shear and compression, observing that in tensile loading, transverse cracking occurred at an early stage before fiber fracture in the longitudinal plies that lead to final fracture; in shear loading, cracks initiated at 0°/90° and 45° to the fiber axes, with the latter causing final fracture; and in compression loading, it was buckling of the fiber bundles that preceded catastrophic failure. Chen et al. [24] investigated the tensile behavior and failure mechanisms of 3D needled C/C-SiC composites using tensile experiments from room temperature to 2000°C. It was observed that the interfacial strength decreased with increasing temperature, and the corresponding increased fiber pullout lead to a lower tensile elastic modulus but higher strength. Li et al. [25] studied the mechanical behavior of 3D C/C-SiC composites under flexural fatigue loading, observing cracking and interfacial degradation to the tensile side of the neutral axis, with no damage in the compressive region. These studies demonstrate the significant complexity of damage development in C/C-SiC composites. Optimisation of these materials requires a better understanding, and

measurement, of how the as-fabricated microstructure affects the initiation and propagation of damage under mechanical loading.

One effective method to study damage development, particularly in complex microstructures such as composites, is the combination of X-ray computed tomography (XCT) and Digital Volume Correlation (DVC). XCT is a nondestructive method that provides high resolution three-dimensional imaging of the microstructure [26], and it can be applied during mechanical tests to obtain in situ observations of the progression of damage development [27]. The digital images provided by XCT can be analyzed using DVC to measure the full-field displacements and strains; this is particularly useful to detect cracks and can quantify the deformation gradients in the material. Together, XCT and DVC have been applied to study a wide range of materials that includes concrete [28], wood [29], graphite [30], gypsum [31] and SiC-SiC ceramic composites [32]. Very few such studies have been made of C/C-SiC composites. For instance, Hausherr et al. [33] used high-resolution XCT to observe the morphology changes in C/C and C/SiC with each LSI processing step, and some of the authors of this work have previously demonstrated the application of combined XCT/DVC in a study of compressive damage development within a 3D braided C/C-SiC composite, fabricated by GSI [13].

In this study, flexural bending tests have been conducted on 3D braided C/C-SiC composites, which were fabricated using the PIP and GSI methods. High resolution in situ XCT images obtained of four-point bend tests using a laboratory-based X-ray microscope have been analysed by DVC to measure the 3D deformation of the microstructures. The aim was to investigate the effect of the fabrication method on the development of mechanical damage.

2 Experimental

2.1 Material Preparation

Three dimensional, five-directional braided, carbon fabrics (volume fraction ~50%) provided by the Composites Institute of Tianjing Technology University (China) were used to prepare C/C preforms through Chemical Vapor Infiltration (CVI) at 960°C, with propylene and argon used as precursor and carrier diluting gases respectively. Preforms with a density of about 1.40 g/cm³ (after 130 hours of CVI) were used to fabricate C/C-SiC composites by Gaseous Silicon Infiltration [34] at 1700°C. Preforms with density of about 1.08 g/cm³ (after 35 hours of CVI) were used to fabricate composites by the Precursor Infiltration and Pyrolysis method [35] at 1200°C. The final bulk densities of the C/C-SiC composites were 2.20 g/cm³ and 1.75 g/cm³ respectively for the GSI and PIP methods.

The samples for four-point mechanical testing with in situ tomography observation (cuboid specimens, nominally $x \times y \times z$, ~ 25 mm \times 3 mm \times 5 mm) were cut from a plate with original dimensions of 120 mm \times 50 mm \times 5.2 mm by using water-jet cutting (x - z planes) and then a water-cooled diamond saw (0.6 mm blade width) (y - z planes). The x - y surfaces were prepared by metallographic grinding. Specimens for 3-point bend tests were similarly prepared with dimensions 40 mm \times 3 mm \times 5 mm for each material type.

2.2 Mechanical Testing

The three-point bend tests were performed in a 1 kN capacity WDW-100 universal testing machine (Changchun Research Institute of Testing Machines, Jilin, China), with a crosshead displacement speed of 0.5 mm/min and a loading span of 30 mm. The four-point bend tests (inner span 6 mm, outer span 20 mm) were done with a Deben CT5000 loading rig (5 kN load capacity, glassy carbon loading pins) that was mounted within an Xradia Versa 510 X-ray microscope, operated at 80 keV energy and 7 W power. The actual sample dimensions ($x \times y \times z$) were 25 mm \times 3.1 mm \times 5.1 mm

and $25\text{ mm} \times 3.0\text{ mm} \times 5.1\text{ mm}$ for the GSI and PIP samples, respectively; this is the maximum dimension of bend specimen that can be tested within the constraints of the Deben loading rig, which is designed for in situ high resolution tomography¹. Each tomograph was reconstructed from 1601 projections recorded over a 360° rotation, with tomographs obtained from a pre-load of 5 N and then at progressively higher loads, with the applied crosshead displacement held constant during each observation. To reduce the time requirement, each radiograph employed 2x binning of the 2048×2048 pixel camera to obtain a 1024×1024 pixel image, with a final image pixel size of $11.5\text{ }\mu\text{m}$. Each tomography scan required about 2 hours and 40 minutes, and a region of interest around the position of maximum bending (Figure 1a) was observed. The attenuation contrast tomographs were reconstructed using the instrument software, without any correction for the material outside of the region of interest. These were cropped to dimensions of $\sim 9.66\text{ mm} \times 2.95\text{ mm} \times 4.97\text{ mm}$ and $\sim 9.62\text{ mm} \times 2.96\text{ mm} \times 4.90\text{ mm}$ for the GSI and PIP samples respectively (<https://imagej.net/>) [36] and were then visualized using the Avizo 9.3.0 software. Tomographs with a voxel size of $2.5\text{ }\mu\text{m}$ (volume $\sim 2.47\text{ mm} \times 2.53\text{ mm} \times 2.48\text{ mm}$, 80 keV energy, 7 W power, 2x binning, 1601 projections, duration 1.5 hours per scan) were also recorded of the unloaded specimens after failure, without the Deben rig, in order to observe the damage at higher resolution.

The LaVision Davis software (version 8.4.0) was used for the digital volume correlation (DVC) analysis of the $11.5\text{ }\mu\text{m}$ tomographs, after downsampling from 16 bit to 8 bit, with the initial tomograph at 5 N pre-load as the reference and using the FFT (fast Fourier transform) correlation

¹ See <https://deben.co.uk/tensile-testing/μxct/tensile-stages-for-x-ray-ct-tomography/> for details of this standard μXCT loading stage set-up on an Xradia Versa microscope.

algorithm. The small final subset size ($24 \times 24 \times 24$ voxels, 75% overlap, 2 passes) achieved a higher spatial resolution of the displacement field, after iterative analysis by larger subset sizes of $128 \times 128 \times 128$ (75% overlap, 2 passes) and $64 \times 64 \times 64$ (75% overlap, 2 passes). The resulting data volumes were cropped to approximately $9.16 \text{ mm} \times 2.60 \text{ mm} \times 4.69 \text{ mm}$ ($796 \times 226 \times 407$ voxels) and $9.23 \text{ mm} \times 2.67 \text{ mm} \times 4.82 \text{ mm}$ ($802 \times 232 \times 418$ voxels) for the GSI and PIP sample, respectively, with potentially inaccurate displacement data removed from subsets that approached the edges of tomographed volume.

3 Results

3.1 Microstructure Characterization

Tomographs obtained at $11.5 \text{ }\mu\text{m}$ voxel resolution in the preloaded condition are shown in Figure 1b and 1c for the GSI and PIP samples; the fiber bundle direction is parallel to the x axis in both. The tomographs are visualisations of the X-ray attenuation coefficient, and the silicon rich SiC has brighter contrast than the carbon fibers due to its higher electron density (i.e. from the combination of higher atomic number elements and physical density), while porosity is observed as black (i.e. low X-ray attenuation). The microstructures are illustrated more clearly in the orthogonal slices in Figure 2. The regions between the fiber bundles of the GSI sample (Figure 2a) are filled with dense SiC matrix, leaving a few near-spherical (inter-bundle) pores between the bundles of fibers. The lower density PIP sample (Figure 2b) has less matrix between the fiber bundles, and significantly more inter-bundle pores that are elongated along the fibers. Initial planar defects (i.e. cracks) within the fiber bundles can be observed in the GSI sample (marked by white arrows in Figure 2a).

The SiC matrix and pores were segmented by greyscale thresholding using the Avizo software. Their 3D visualizations are shown in Figure 3 and their proportions are quantified in Figure 4. The microstructures are quite constant, in terms of matrix and porosity content, along the length of the

tomographed volumes. The GSI sample, with a calculated matrix volume fraction of 41.7 % (Figure 4a), has large regions of inter-bundle matrix (Figure 3a), while the PIP sample exhibits thinner matrix regions (Figure 3b) with a lower matrix volume fraction of 23.6 % (Figure 4a). The total porosity is correspondingly higher in the PIP sample (13.1%) than in the GSI sample (4.5%).

Gravimetric analysis [37] of materials from the same blocks as the tested samples measured a carbon volume fraction of 53% and matrix volume fraction of 42.1% (SiC 22.1%; Si 20.0%) with a porosity of 4.9% for the GSI material, whereas for the PIP material the carbon volume fraction was 61.9%, with a SiC matrix of 21.5% and 16.6% porosity. In the PIP sample, the observed porosity is distributed both within (intra-bundle) and between (inter-bundle) the fiber bundles and is mostly inter-bundle, whereas in the GSI microstructure the observed porosity is predominantly intra-bundle (Figure 4b); the small amount of measured porosity includes the intra-bundle and inter-bundle spherical pores. Scanning electron microscopy was conducted on samples that had been etched in a mixture of nitric and hydrofluoric acids ($\text{HNO}_3:\text{HF}=4:1$) at 40°C to dissolve residual silicon as part of the gravimetric analysis (Figure 4c). In the etched GSI composite, the regions near the inter-bundle region, which is the path for the silicon infiltration, show evidence of greater attack in comparison to the PIP composite; this indicates a greater penetration of silicon and conversion of fibers to SiC in the fiber bundles of the GSI composite.

3.2 Observation of Damage Development

Mechanical test data for the ex situ three-point bend tests are shown in Figure 5a. They are presented as flexural stress vs. crosshead displacement to remove the effects of small differences (<6%) in specimen cross-section dimensions. The mean flexural strengths, obtained from the peak loads, were 140 ± 7 MPa and 344 ± 36 MPa for GSI and PIP. The respective flexural moduli, obtained by a regression fit to the linear region below 50% of the peak load, were 59 ± 4 GPa and 66 ± 10 GPa. The load-crosshead displacement data for the in situ four-point flexural tests are shown in Figure 5b,

in which open circles indicate the positions at which tomographs were recorded. A small load relaxation occurred during each scan (less than $\sim 9.5\%$). The maximum loads were 336 N and 470 N, respectively (i.e. peak flexural stresses in the x -direction of the x - z surface plane of 137 and 210 MPa). In all tests, quasi-brittle fracture was observed in both the GSI and PIP materials.

Scanning electron microscopy of fracture surfaces from the four-point bend tests (Figure 6) show significant roughness due to convoluted crack paths. This is particularly the case for the PIP composite, in which the fracture has propagated between the fiber bundles to a much greater degree than the GSI composite. The degree of fiber pullout is also much greater in the PIP composite than for the GSI composite.

Tomographs recorded after the peak load in the four-point bend tests, at voxel size of $11.5\ \mu\text{m}$, are shown in Figure 7, with the locations of the loading pins marked by white dashed lines. Both the GSI and PIP samples have developed a dominant crack at this stage. In the GSI sample, the crack is approximately orthogonal to the x -axis, propagating across the fiber bundles and matrix, whereas in the PIP sample the dominant crack is inclined to the x -axis and tends to follow the matrix/fiber bundle interfaces. This is shown more clearly in the unloaded higher resolution ($2.5\ \mu\text{m}$ voxel) tomographs (Figure 8). In these, fiber fractures and inter-bundle cracking can be clearly observed within the GSI sample (Figure 8a), while in the PIP sample the cracks that follow the matrix/fiber bundle interface are mostly within the SiC matrix (Figure 8b). The higher resolution tomographs also confirm that the PIP microstructure has both higher inter- and intra-bundle porosity than the GSI.

The sequence of damage development is illustrated in Figure 9, which shows x - y plane slices from the same position in the tomographs ($z=2.80\ \text{mm}$). In both GSI and PIP samples, cracks started from the tensile region (bottom of the images); there is no apparent damage in the compressive region of the GSI sample although intra-bundle cracking can be observed in the compressive region of the PIP sample after the peak load (see Figure 9b, Failed). In the GSI sample, new cracks are first observed

from 200 N. A typical example is highlighted by a white dotted box at 200 N (Figure 9a), in which the crack runs across a fiber bundle. The final dominant crack, which is highlighted within the dashed white box (A), propagated across the matrix and fiber bundles and took a path that both followed and crossed the fibers. No new damage was observed until 350 N in the PIP sample (Figure 9b). As shown in the selected box (B), the fracture of the PIP sample tended to propagate along the fiber bundle/matrix interface, with the damage in the fiber bundle tending to follow the fiber interfaces.

The strong attenuation contrast of the cracks in the tomographs allow their segmentation, and the 3D development of cracking with increasing load is visualized in Figure 10. This illustrates the pattern of pre-existing predominantly intra-bundle cracks (green color) in the GSI sample (Figure 10a), which increased in number and dimension with increasing load. New cracks (red) are also shown that have initiated perpendicular to the applied stress at different positions, and propagated from the tensile region to cause the final failure; these had little interaction with the pre-existing defects in the microstructure. There were no significant initial cracks observable for the PIP sample (Figure 10b), and the damage (blue) evolved to predominantly follow the interfaces between the matrix and fiber bundles. These cracks can be observed within both the tensile and compressive regions of the specimen, but are predominantly within the tensile region.

3.3 Digital Volume Correlation Analysis of Deformation

The flexural deformation of the specimens was quantified by considering the change in the x displacement between the two vertical (y - z) planes beneath the loading pins, which are separated by a distance of 6 mm. The displacements were normalized by the bending moment at each load and are visualised in Figure 11, which shows that although the data at lower loads are more scattered due to the smaller displacements in comparison to measurement errors, the composites exhibit uniform flexure across the z -axis. The average values along the z axis, as a function of y , are thus shown in

Figure 12(a and b), with the standard deviation at each y -position represented by the error bars. In Figure 11, the position of the neutral axis moves from the midpoint and away from the tensile (lower) surface at 300 N in the GSI sample, and at 450 N in the PIP sample. The quantification in Figure 12 is more sensitive and shows the movement of the neutral axis and steepening of the displacement gradient at 200 N in the GSI, and from 300 N in the PIP.

A simple Euler–Bernoulli (slender beam, linear homogeneous elastic properties) analysis was used to estimate the apparent elastic moduli of the two composites as a function of increasing load. The analysis neglects the movement of the neutral axis that is observed in Figure 11, and uses the linear gradient of the strain, $\frac{d\epsilon_x}{dy}$, to provide its radius of curvature, R , thus:

$$M = EI/R \text{ and } \frac{d\epsilon_x}{dy} = -1/R \quad (1)$$

Where M is the bending moment, I is the second moment of area of the beam and E is the elastic modulus. The bending moment that caused the measured deformation is obtained from the applied load and four-point bending geometry, treating the small 5 N preload as negligible. The strain gradient is calculated using a linear regression analysis of the average strains, which are obtained from the measured change in displacement, Δx , over the 6 mm distance between the loading points; all the data that are represented by the ± 1 standard deviation error bars of Figure 12(a and b) are considered, and the standard deviation of the best fit gradient is better than 2%. This analysis (Figure 12c) finds that the apparent elastic modulus of the PIP composite decreased progressively from 101 ± 2.1 GPa to 36 ± 0.4 GPa; the most significant change occurred above 200 N applied load. The smaller number of observations of the GSI composite show a continuous fall in apparent modulus from 119 ± 2.5 GPa to 38 ± 0.5 GPa.

The DVC data have also been used to calculate the displacement difference in the y direction, between the two (x - z) planes close to the top ($y_2=2.81$ mm) and bottom ($y_1=0.15$ mm) of the

specimen. The data are shown as strain maps in Figure 13, where the average through-thickness strain was calculated by normalizing the displacement difference by the distance (2.66 mm) between the measurement planes. The GSI sample (Figure 13a) shows an elongated pattern of through-thickness strain that is aligned with the fiber bundle direction; it changes significantly at 300 N with a reversal in sign at some locations. The PIP sample (Figure 13b) shows a progressive and localized increase in through-thickness strain from 300 N.

3.4 Discussion

These tomography observations of the initial microstructures (Figure 1 and Figure 2) show that the GSI process produces a more compact and dense structure than the PIP process, in which the distribution of the resulting SiC matrix is controlled by its growth from the surface of fiber bundles (Figure 3). The observed proportions of matrix and porosity are quite consistent with the gravimetric analysis, although the limited resolution of the tomographs has not allowed measurement of finer pores, so the total observed porosity is an underestimate of the full porosity. The infiltration of silicon into the GSI sample filled not only the inter-bundle regions of the braided preform, but also the fiber bundles (Figure 8) to achieve a low intra-bundle porosity (Figure 4b). This is confirmed by the etching behaviour of the intra-bundle regions (Figure 4c), which reveals the penetration of silicon. The increased resistance to fiber pullout (Figure 6) in the GSI composite, compared to PIP, is also consistent with partial conversion of the fibers to SiC, which would increase the shear resistance of the fiber-matrix interface.

In comparison with surface imaging techniques such as optical and scanning electron microscopy, the significant advantage of XCT observation as the specimens are loaded is that it allows study of the progressive development of damage within the material. It also gives confidence that none of the observed damage was introduced by destructive specimen preparation. This study confirms that the pre-existing internal defects in the GSI composite were predominantly intra-bundle cracks (Figure 9).

Internal cracks are expected to be more prevalent in the GSI composite since the high process temperature, in comparison to PIP, would increase the thermal strains between matrix and fibers that are due to their significant difference of transverse thermal expansion coefficient [38]. Similar process-induced cracks, which were proposed to contribute to a reduction in Young's modulus, have been reported previously in the matrix of two-dimensional C-SIC composites fabricated by LSI [11]. However, this is the first time that the three-dimensional distribution of such internal cracks, and their development, has been visualised. The fracture of the GSI composite did not interact significantly with these cracks, and the low strength of the GSI composite arises from the lack of resistance to crack propagation compared to the PIP composite in which crack deflection and fiber pullout are significant due to the weak fiber-matrix interface.

The GSI and PIP composites were fabricated from the same preform, so from simple mechanical considerations [39] the higher density GSI composite would be expected to have higher stiffness. This is not observed in the three-point or four-point bending behaviours (Figure 5) that are described by the relationships between load and applied crosshead displacement; the GSI appears more compliant than the PIP. However, advantage can be taken of the in situ observations by XCT and DVC to measure the actual deformations of the four-point bend specimens (Figure 11 and Figure 12).

In the linear elastic analysis of the specimen curvatures, the initial apparent elastic moduli of the PIP and GSI composites were 101 ± 2.1 GPa and 119 ± 2.5 GPa respectively. These measurements of elastic properties, which were obtained by direct measurement of the specimen deformation, are significantly higher than calculated using the load and crosshead displacement data. It should be noted that the applied crosshead displacements in the elastic regime (i.e. below 50% of peak load) are very small; less than 100 μm for GSI and 200 μm for PIP. The transverse elastic modulus (perpendicular to the fiber direction) in the GSI composite is low, due to the low transverse stiffness of the carbon fibers in the braided structure, and has been measured to be ~ 20 GPa [13]. A similarly

low transverse modulus would be expected also in the PIP composite, which is fabricated from the same carbon fiber preform. Transverse compression of the specimens due to low transverse stiffness will add to the crosshead displacements, particularly in short bend specimens that require high loads to obtain a significant flexural stress, and this would reduce the apparent flexural stiffness (Figure 5). The flexural moduli obtained in the three and four-point bend tests using load and crosshead displacement data are therefore not reliable, and would not be reliable even if the load-line displacements were measured directly at the specimen. Standardised flexural tests for ceramic composites [40] require a span to thickness ratio in excess of 15. This is primarily to avoid shear effects, which were not observed in these tests, but a high span to thickness ratio would also reduce contact loads, and so diminish the effects of transverse compression on the load-displacement behaviour in these anisotropic materials.

There are currently no published data for the tensile elastic moduli of these GSI and PIP composites, but there are data for composites with similar constituents; the tensile modulus of T300 carbon fiber is ~ 230 GPa [41] and the typical modulus of SiC produced by the GSI process is ~ 200 GPa [42]. In a two-dimensional LSI-fabricated C-SiC composite with 40% fiber content, the highest tensile modulus was 145 GPa; lower values were attributed to the effects of thermal residual stresses [11]. A high tensile modulus of 130 GP was obtained in a CVI-fabricated two-dimensional C-SiC composite (40% fiber content) [39], although a study of a similar composite achieved a modulus of 94 GPa [43], and values from 60 GPa to 75 GPa have been reported for lower density CVI processed C-SiC composites with needle-stitched $0^\circ/90^\circ$ carbon fiber preforms [44,45]. In all these studies, the tensile modulus decreased with increasing tensile strain. In the flexural loading of the GSI and PIP composites in this study, up to half of the specimen cross-section is under compression (Figure 11); this would act to close any pre-existing internal cracks that would then have a lesser effect on the stiffness. A previous study, which examined the longitudinal compressive behaviour of the same GSI material, obtained a lower-bound estimate of 160 GPa [13]. The flexural moduli of ~ 100 to 120

GPa (Figure 12c) obtained in this study by DVC of tomographs are therefore reasonable. The initial stiffness (Figure 12c) of the GSI is ~18% greater than that of the PIP, and this trend is consistent with their observed 26% difference in porosity (Figure 4a).

If the flexural deformation followed simple beam theory with constant linear elastic modulus (i.e. constant flexural rigidity), then the normalized displacements (Figure 12) should have a constant gradient, with the zero value of the neutral axis at the specimen midsection (i.e. at $y \sim 1.5$ mm). The data show a changing gradient and a movement of the neutral axis with increasing load, which means that the curvature of the specimen has increased above that expected for its flexure at constant elastic modulus. Similarly, for elastic deformation in four-point bending with constant modulus, the through-thickness strains (Figure 13) should be small and approximately constant. The observed changes therefore reveal the effects of intra- and inter-bundle cracking, which increase the total strain and reduce the effective elastic modulus in tension. The inter-bundle splitting of the PIP sample (Figure 7) is very evident (Figure 13b), and the opening of intra-bundle cracks in the GSI sample caused a pattern of displacements that reveal the heterogeneous microstructure.

The use of tomography and DVC to effectively strain gauge the microstructure shows that there is change in the flexural rigidity of the composites with increasing load. This is due to the reduction in elastic modulus in the tensile region that is caused by an increase in the proportion of open cracks in the microstructure with increasing tensile strain (Figure 10). The behavior is similar to that of a functionally-graded material [46] in which a reduced elastic modulus can act to lower the surface stresses in the microstructure and increase strength; in this case, the apparent modulus is reduced due to the effects of crack development [47] and is thus a function of the applied strain. In principal, a more detailed analysis of the three-dimensional displacement field with increasing bending moment, such as with the finite element method, could be used to quantify the material relationship between tensile strain and elastic modulus to support composite design. A more extensive study, utilizing

tomographs recorded both under load, and after full or partial unloading, would be necessary to separate unambiguously the effects of cracking from inelastic deformation [30].

This study has shown that DVC measurements from tomographs can provide unambiguous observations of deformation that identify the onset of mechanical damage. Combined studies using XCT and DVC can therefore be used to reliably quantify the effects of mechanical loading on damage development and the flexural properties of braided ceramic composites. This approach would be applicable to other material systems, including ceramic composites with different preforms, and also those in which complex structural modifications such as short-cut webs and needle stitching are introduced. The combined XCT/DVC approach may also be extended to more complex stress states and cyclic loading. Ultimately, measurements of the evolution of the displacement field may also be used to verify numerical models for damage development, which can aid the optimal design of composites [48,49].

4 Conclusion

The flexural behaviour of 3-dimensional 5-directional braided C/C-SiC ceramic composites produced by the GSI and PIP methods from the same preform have been studied in situ, for the first time, with laboratory X-ray computed tomography (XCT). Measurements of the internal displacement field by digital volume correlation (DVC) show that both composites experience a progressive degradation of flexural modulus with increasing tensile strain that is due to mechanical damage by crack propagation. The GSI composite has higher density, which gives it an initially higher stiffness than the PIP composite. The GSI composite has a significant intrinsic population of intra-bundle crack-like defects due to its high processing temperature, and a lower tendency for fiber pullout. Consequently its strength is lower than the composite produced by PIP.

5 Acknowledgements

We acknowledge EPSRC Grant EP/M02833X/1 “University of Oxford: experimental equipment upgrade” that supported the Xradia Versa 510 microscope and facilities for data analysis and visualization. The research is part of the Project 2018JJ1029 supported by Hunan Provincial Natural Science Foundation of China. The work was conducted at Oxford University, with China Scholarship Council support for Wan Fan as a recognized student.

6 References

- [1] W. Krenkel, F. Berndt, C/C-SiC composites for space applications and advanced friction systems, *Materials Science and Engineering A*. 412 (2005) 177–181. doi:10.1016/j.msea.2005.08.204.
- [2] M. Patel, K. Saurabh, V. Prasad, J. Subrahmanyam, High temperature C/C-SiC composite by liquid silicon infiltration: A literature review, *Bulletin of Materials Science*. 35 (2012) 67–77. doi:10.1007/s12034-011-0247-5.
- [3] Z. Cheng, D. Shi, X. Jing, X. Yang, An exploration of structure design in 3D braided ceramic matrix composites turbine blade dovetail attachment, In: 21th International Conference on Composite Materials, Xi'an, PR China, Chinese Society for Composite Materials, (2017) 20–25.
- [4] X. Zhou, D. Zhu, Q. Xie, F. Luo, W. Zhou, Friction and wear properties of C/C-SiC braking composites, *Ceramics International*. 38 (2012) 2467–2473. doi:10.1016/j.ceramint.2011.11.015.
- [5] Z. Li, P. Xiao, B. Zhang, Y. Li, Y. Lu, Preparation and tribological properties of C/C-SiC brake composites modified by in situ grown carbon nanofibers, *Ceramics International*. 41 (2015) 11733–11740. doi:10.1016/j.ceramint.2015.05.139.
- [6] C. Shih, Y. Katoh, L. Snead, J. Steinbeck, The effect of neutron irradiation on the mechanical properties of C/SiC composites, *Journal of Nuclear Materials*. 439 (2013) 192–201. doi:10.1016/j.jnucmat.2013.03.089.
- [7] B. Heidenreich, W. Krenkel, B. Lexow, Development of CMC-materials for lightweight armor, in: 27th Annual Cocoa Beach Conference on Advanced Ceramics and Composites: A: Ceramic Engineering and Science Proceedings, USA, Wiley-Blackwell, (2008) 375–381. doi:10.1002/9780470294802.ch55.
- [8] D. Li, Z. Lu, L. Chen, J. Li, Microstructure and mechanical properties of three-dimensional five-directional braided composites, *International Journal of Solids and Structures*. 46 (2009) 3422–3432. doi:10.1016/j.ijsolstr.2009.05.013.
- [9] D. Li, Z. Lu, D. Fang, Longitudinal compressive behavior and failure mechanism of three-dimensional five-directional carbon/phenolic braided composites at high strain rates, *Materials Science and Engineering A*. 526 (2009) 134–139. doi:10.1016/j.msea.2009.07.009.
- [10] D. Zhang, L. Chen, Y. Sun, X. Wang, Transverse tensile damage behaviors of three-dimensional five-directional braided composites by meso-scale finite element approach, *Journal of Reinforced Plastics and Composites*. 34 (2015) 1202–1220. doi:10.1177/0731684415587350.
- [11] X. Fan, X. Yin, X. Cao, L. Chen, L. Cheng, L. Zhang, Improvement of the mechanical and thermophysical properties of C/SiC composites fabricated by liquid silicon infiltration, *Composites Science and Technology*. 115 (2015) 21–27.

doi:10.1016/j.compscitech.2015.04.019.

- [12] B. Li, J. Zhu, L. Lin, Y. Liu, Z. Chen, Fracture mechanism of 3D, five-directional braided (SiO₂)_f/SiO₂ composites prepared by silicasol-infiltration- sintering method, *Journal Wuhan University of Technology, Materials Science Edition*. 28 (2013) 355–357. doi:10.1007/s11595-013-0694-5.
- [13] F. Wan, S. Zhao, R. Liu, C. Zhang, T.J. Marrow, In situ observation of compression damage in a three-dimensional braided carbon fiber reinforced carbon and silicon carbide (C/C-SiC) ceramic composite, *Microscopy and Microanalysis*. 24 (2018) 227–237. doi:10.1017/S1431927618000351.
- [14] Y. Xiang, W. Li, S. Wang, Z. Chen, Oxidation behavior of oxidation protective coatings for PIP-C/SiC composites at 1500 °C, *Ceramics International*. 38 (2012) 9–13. doi:10.1016/j.ceramint.2011.06.063.
- [15] H. Wang, D. Zhu, F. Wan, W. Zhou, F. Luo, Influence of the C/C preform density on tribological characteristics of C/C-SiC composites under different conditions, *Ceramics International*. 40 (2014) 16641–16646. doi:10.1016/j.ceramint.2014.08.025.
- [16] D. Huang, M. Zhang, Q. Huang, L. Wang, L. Xue, X. Tang, K. He, Ablation mechanism of C/C-ZrB₂-ZrC-SiC composite fabricated by polymer infiltration and pyrolysis with preform of C_f/ZrB₂, *Corrosion Science*. 98 (2015) 551–559. doi:10.1016/j.corsci.2015.05.064.
- [17] S. Jiang, X. Xiong, Z. Chen, P. Xiao, B. Huang, Influence factors of C/C-SiC dual matrix composites prepared by reactive melt infiltration, *Materials and Design*. 30 (2009) 3738–3742. doi:10.1016/j.matdes.2009.02.013.
- [18] P. Xiao, Z. Li, X. Xiong, Microstructure and tribological properties of 3D needle-punched C/C-SiC brake composites, *Solid State Sciences*. 12 (2010) 617–623. doi:10.1016/j.solidstatesciences.2010.01.014.
- [19] Q. Zhou, S. Dong, X. Zhang, Y. Ding, D. Jiang, Fabrication of C_f/SiC composites by vapor silicon infiltration, *Journal of the American Ceramic Society*. 89 (2006) 2338–2340. doi:10.1111/j.1551-2916.2006.01018.X.
- [20] H. Wang, X. Zhou, J. Yu, Y. Cao, R. Liu, Fabrication of SiC_f/SiC composites by chemical vapor infiltration and vapor silicon infiltration, *Materials Letters*. 64 (2010) 1691–1693. doi:10.1016/j.matlet.2010.05.013.
- [21] H. Xiao, Y. Lu, W. Zhao, X. Qin, The effect of heat treatment temperature and time on the microstructure and mechanical properties of PAN-based carbon fibers, *Journal of Materials Science*. 49 (2014) 794–804. doi:10.1007/s10853-013-7762-2.
- [22] B. Swaminathan, A. Painuly, P. V. Prabhakaran, S. Packirisamy, Liquid polycarbosilane-derived C/C-SiC composites with improved mechanical strength for high temperature applications, *Ceramics International*. 41 (2015) 3574–3577. doi:10.1016/j.ceramint.2014.10.185.
- [23] N. Weigel, B. Kröplin, D. Dinkler, Micromechanical modeling of damage and failure

- mechanisms in C/C–SiC, *Computational Materials Science*. 16 (1999) 120–132. doi:10.1016/S0927-0256(99)00054-3.
- [24] Z. Chen, G. Fang, J. Xie, J. Liang, Experimental study of high-temperature tensile mechanical properties of 3D needled C/C–SiC composites, *Materials Science and Engineering: A*. 654 (2016) 271–277. doi: 10.1016/j.msea.2015.12.010.
- [25] Y. Li, P. Xiao, Y. Shi, R. Almeida, W. Zhou, Z. Li, H. Luo, F. Reichert, N. Langhof, W. Krenkel, Mechanical behavior of LSI based C/C–SiC composites subjected to flexural loadings, *Composites Part A: Applied Science and Manufacturing*. 95 (2017) 315–324. doi:10.1016/j.compositesa.2017.01.024.
- [26] C. Zou, T.J. Marrow, C. Reinhard, B. Li, C. Zhang, S. Wang, Porosity characterization of fiber-reinforced ceramic matrix composite using synchrotron X-ray computed tomography, *Journal of Instrumentation*. 11 (2016) C03052. doi:1748-0221/11/i=03/a=C03052.
- [27] J. Marrow, C. Reinhard, Y. Vertyagina, L. Saucedo-Mora, D. Collins, M. Mostafavi, 3D studies of damage by combined X-ray tomography and digital volume correlation, *Procedia Materials Science*. 3 (2014) 1554–1559. doi:10.1016/j.mspro.2014.06.251.
- [28] Z. Yang, W. Ren, R. Sharma, S. McDonald, M. Mostafavi, Y. Vertyagina, T.J. Marrow, In-situ X-ray computed tomography characterisation of 3D fracture evolution and image-based numerical homogenisation of concrete, *Cement and Concrete Composites*. 75 (2017) 74–83. doi: 10.1016/j.cemconcomp.2016.10.001.
- [29] F. Forsberg, R. Mooser, M. Arnold, E. Hack, P. Wyss, 3D micro-scale deformations of wood in bending: Synchrotron radiation μ CT data analyzed with digital volume correlation, *Journal of Structural Biology*. 164 (2008) 255–262. doi: 10.1016/j.jsb.2008.08.004.
- [30] T.J. Marrow, D. Liu, S.M. Barhli, L. Saucedo Mora, Y. Vertyagina, D.M. Collins, C. Reinhard, S. Kabra, P.E.J. Flewitt, D.J. Smith, In situ measurement of the strains within a mechanically loaded polygranular graphite, *Carbon*. 96 (2016) 285–302. doi: 10.1016/j.carbon.2015.09.058.
- [31] A. Bouterf, S. Roux, F. Hild, J. Adrien, E. Maire, S. Meille, M. De Lyon, B.B. Pascal, A.J. Capelle, V. Cedex, S. Recherche, L. Lefranc, A. Cedex, Digital volume correlation applied to x-ray tomography images from spherical indentation tests on lightweight gypsum, *C* (2014) 444–453. doi:10.1111/str12101.
- [32] L. Saucedo-Mora, T. Lowe, S. Zhao, P.D. Lee, P.M. Mummery, T.J. Marrow, In situ observation of mechanical damage within a SiC–SiC ceramic matrix composite, *Journal of Nuclear Materials*. 481 (2016) 13–23. doi: 10.1016/j.jnucmat.2016.09.007.
- [33] J.M. Hausherr, W. Krenkel, F. Fischer, V. Altstädt, Nondestructive characterization of high - performance c/sic - ceramics using x - ray - computed tomography. *International Journal of Applied Ceramic Technology* (2010) 7 361-368. doi:10.1111/j.1744-7402.2009.02449.x
- [34] L. Huang, R. Liu, C. Zhang, Y. Wang, Y. Cao, Si/SiC optical coatings for C/SiC composites via gel-casting and gas silicon infiltration: Effects of carbon black content, *Journal of Alloys and Compounds*. 711 (2017) 162–168. doi:10.1016/j.jallcom.2017.03.222.

- [35] X. Yang, H. Hu, Y. Zhang, Z. Chen, Thermal shock properties of 3D-C/SiC composites prepared via polymer infiltration pyrolysis (PIP), *Ceramics International*. 40 (2014) 9087–9094. doi:10.1016/j.ceramint.2014.01.122.
- [36] C.A. Schneider, W.S. Rasband, K.W. Eliceiri, NIH Image to ImageJ: 25 years of image analysis, *Nature Methods*. 9 (2012) 671–675. doi:10.1038/nmeth.2089.
- [37] J. Nie, Y. Xu, L. Zhang, S. Fan, F. Xu, L. Cheng, J. Ma, X. Yin, Microstructure, thermophysical, and ablative performances of a 3D needled C/C-SiC composite, *International Journal of Applied Ceramic Technology*. 7 (2010) 197–206. doi:10.1111/j.1744-7402.2008.02341.x.
- [38] C. Pradere, C. Sauder, Transverse and longitudinal coefficient of thermal expansion of carbon fibers at high temperatures (300–2500 K), *Carbon*. 46 (2008) 1874–1884. doi:10.1016/j.carbon.2008.07.035.
- [39] C. Yang, L. Zhang, B. Wang, T. Huang, G. Jiao, Tensile behavior of 2D-C/SiC composites at elevated temperatures: Experiment and modeling, *Journal of the European Ceramic Society*. 37 (2017) 1281–1290. doi:10.1016/j.jeurceramsoc.2016.11.011.
- [40] D7264/D7264M-06, Standard test method for flexural properties of continuous fiber-reinforced advanced ceramic composites, *ASTM Book of Standards*. 15 (2010) 1–11. doi:10.1520/D3039_D3039M-08.
- [41] H. Miyagawa, T. Mase, C. Sato, E. Drown, L. Drzal, K. Ikegami, Comparison of experimental and theoretical transverse elastic modulus of carbon fibers, *Carbon*. 44 (2006) 2002–2008. doi:10.1016/j.carbon.2006.01.026.
- [42] L. Huang, R. Liu, Y. Wang, C. Zhang, X. Long, Y. Cao, Fabrication and properties of dense silicon carbide ceramic via gel-casting and gas silicon infiltration, *Ceramics International*. 42 (2016) 18547–18553. doi:10.1016/j.ceramint.2016.08.194.
- [43] H. Mei, Q. Bai, H. Li, C. Yu, L. Cheng, Effect of loading rate and temperature on monotonic tensile behavior in two-dimensional C/SiC composites, *Ceramics International*. 40 (2014) 16635–16640. doi:10.1016/j.ceramint.2014.08.024.
- [44] Z. Chen, G. Fang, J. Xie, J. Liang, Experimental study of high-temperature tensile mechanical properties of 3D needled C/C-SiC composites, *Materials Science and Engineering A*. 654 (2016) 271–277. doi:10.1016/j.msea.2015.12.010.
- [45] J. Nie, Y. Xu, L. Zhang, L. Cheng, Microstructure and tensile behavior of multiply needled C/SiC composite fabricated by chemical vapor infiltration, *Journal of Materials Processing Technology*. 209 (2009) 572–576. doi:10.1016/j.jmatprotec.2008.02.035.
- [46] B. Koohbor, S. Mallon, A. Kidane, A. Anand, V. Parameswaran, Through thickness elastic profile determination of functionally graded materials, *Experimental Mechanics*. 55 (2015) 1427–1440. doi:10.1007/s11340-015-0043-z.
- [47] S. Barhli, L. Saucedo-Mora, M. Jordan, A. Cinar, C. Reinhard, M. Mostafavi, T.J. Marrow, Synchrotron X-ray characterization of crack strain fields in polygranular graphite, *Carbon*. 124

(2017) 357–371. doi: 10.1016/j.carbon.2017.08.075.

- [48] L. Saucedo-Mora, C. Zou, T. Lowe, T.J. Marrow, Three-dimensional measurement and cohesive element modelling of deformation and damage in a 2.5-dimensional woven ceramic matrix composite, *Fatigue & Fracture of Engineering Materials & Structures*. 40 (2016) 683–695. doi:10.1111/ffe.12537.
- [49] L. Saucedo-Mora, T.J. Marrow, Multi-scale damage modelling in a ceramic matrix composite using a finite-element microstructure meshfree methodology, *Philosophical Transactions Royal Society A*. 374 (2016) 1–15.

7 Figure Captions

Figure 1: Set up of in situ four-point bending test. (a) schematic diagram; 3D visualization of observed region of (b) GSI sample and (c) PIP sample.

Figure 2: Tomograph cross-sections (11.5 μm voxel) from Figure 1 to show the microstructure of (a) GSI sample and (b) PIP sample. Intra-bundle cracks are indicted by white arrows.

Figure 3: Microstructure 3D visualization. (i) matrix, (ii) total porosity and (iii) inter fiber bundle pores of (a) GSI sample and (b) PIP sample.

Figure 4: Quantitative measurement of microstructure by image segmentation of 11.5 μm voxel tomographs: (a) area fractions of pore and matrix along x axis and (b) the porosity ratios of inter bundle and intra bundle pores to the total measured porosity; (c) Scanning electron microscopy (SEM) characterization of acid etched surfaces; (i) GSI and (ii) PIP.

Figure 5: Mechanical testing data for GSI and PIP materials: (a) flexural stress vs. displacement for the three-point bending; (b) applied load vs. displacement for the tomographed specimens in four-point bending. The points at which tomography (11.5 μm voxel) was performed are indicated.

Figure 6: Scanning electron microscopy (SEM) fractography of a) GSI and b) PIP four-point bend specimens.

Figure 7: Damage visualization using tomography (11.5 μm voxel) of (a) GSI and (b) PIP samples after failure; (i) 3D volumes and orthogonal slices parallel to (ii) x - z plane and (iii) x - y plane. Common lines A-A and B-B are indicated. The y - x planes below the loading pins are marked by white dotted lines.

Figure 8: Sections (x - y plane) of high resolution tomographs, after failure, (2.5 μm voxel) of (a) GSI and (b) PIP samples.

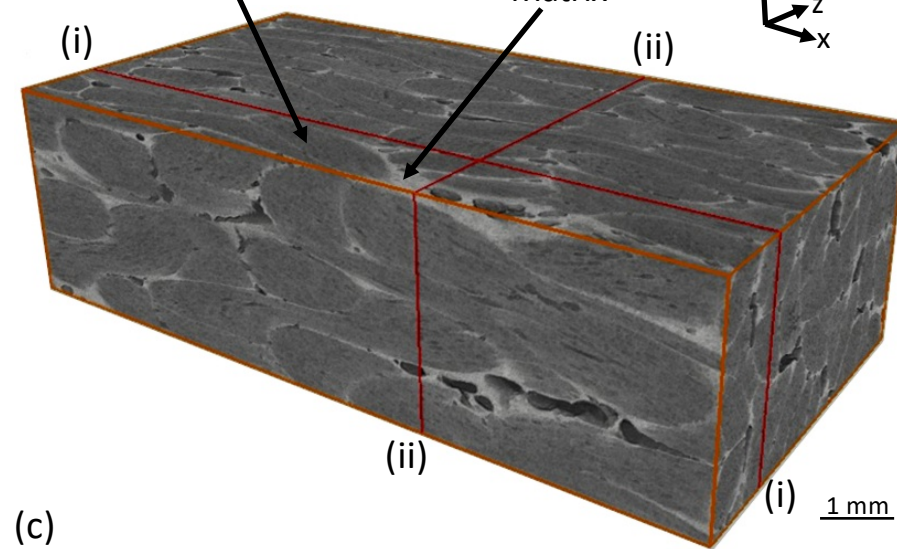
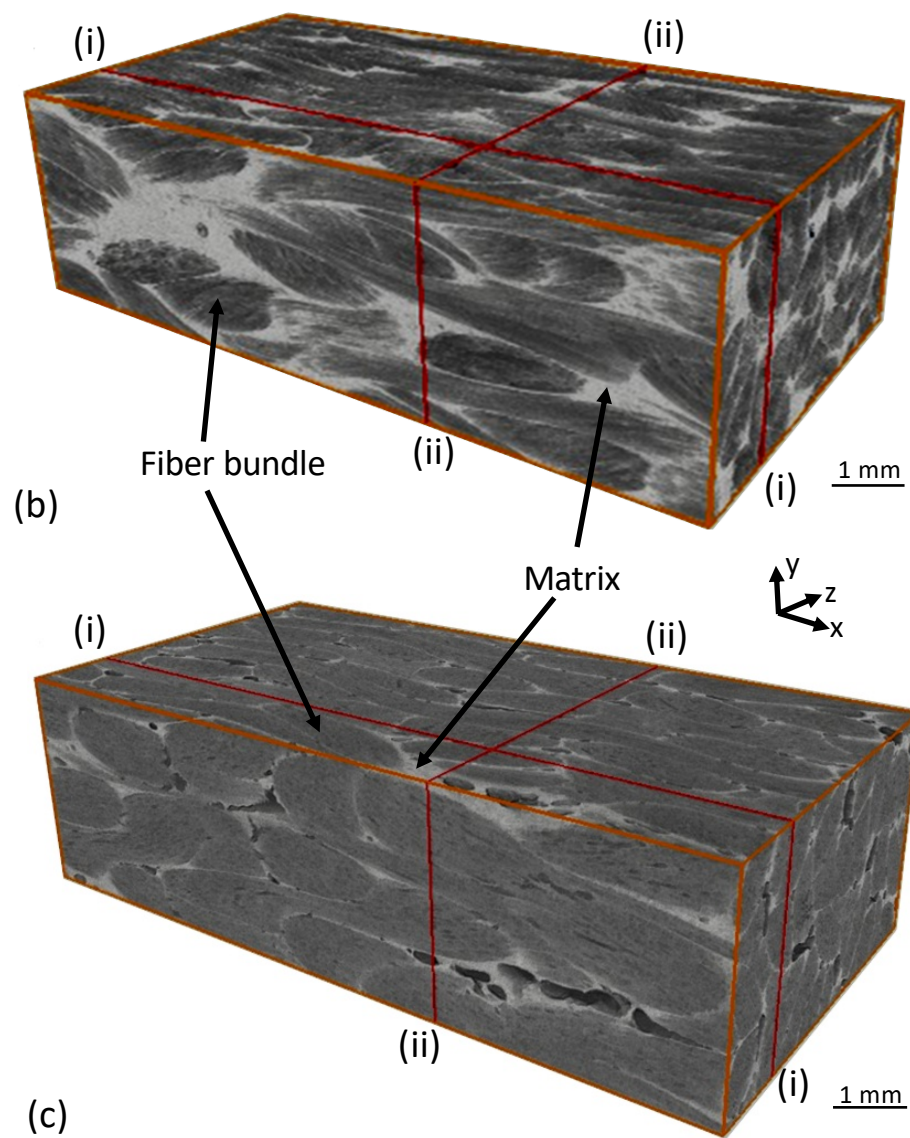
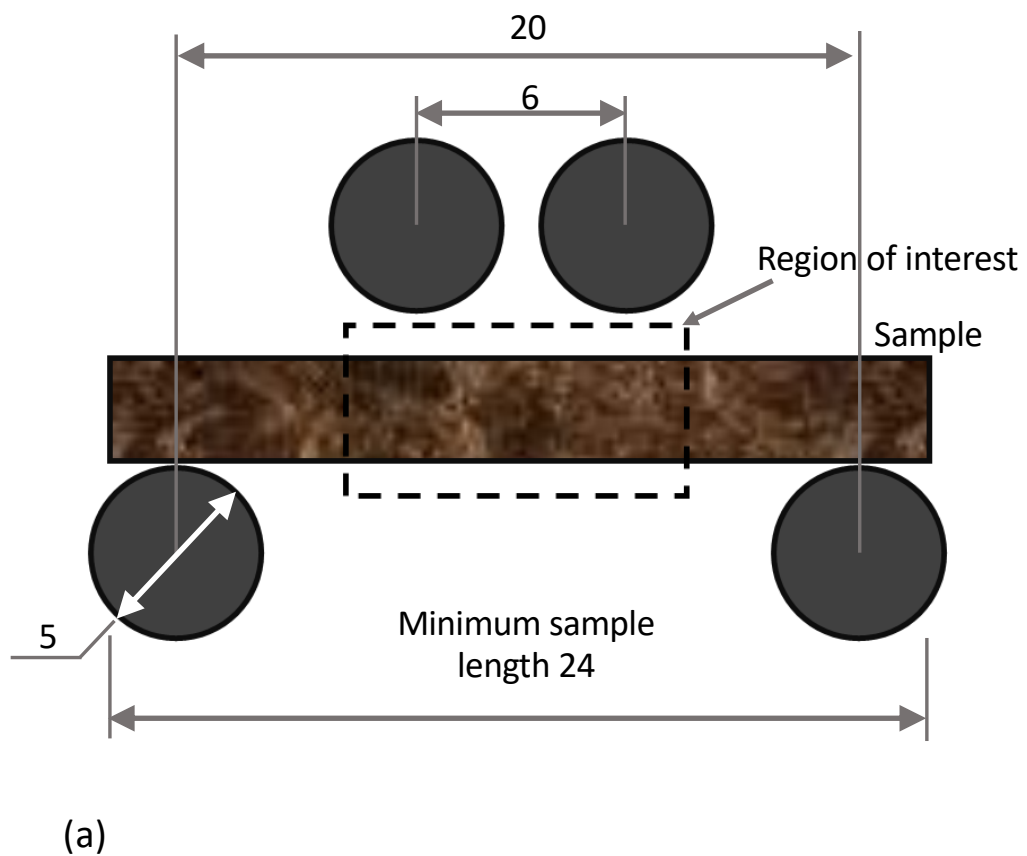
Figure 9: The sequence of crack development with increasing load, observed in the x - y sections of (a) GSI and (b) PIP samples. The locations of the y - z planes beneath the loading pins are marked by white dashed lines.

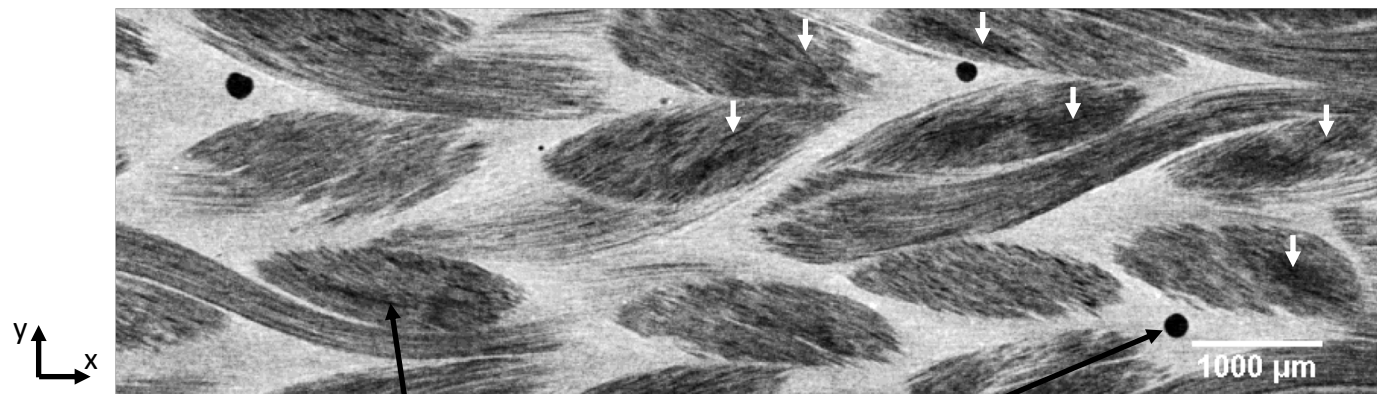
Figure 10: 3D visualization of crack development with increasing loads of (a) GSI and (b) PIP samples. The y - z planes at the loading points are marked by black dashed lines. In (i) to (iv), the tensile flexural surface is at the bottom of the image, and in (v) the volume is viewed from the bottom surface.

Figure 11: Maps of the evolution with increasing load of the x -displacement difference between the y - z planes at the loading points (normalized by applied bending moment) for (a) GSI and (b) PIP samples.

Figure 12: Data from Figure 11, averaged along z axis and plotted as a function of y for (a) GSI and (b) PIP samples. Error bars are the standard deviations; c) the apparent elastic moduli, obtained from the measured strain gradient and load.

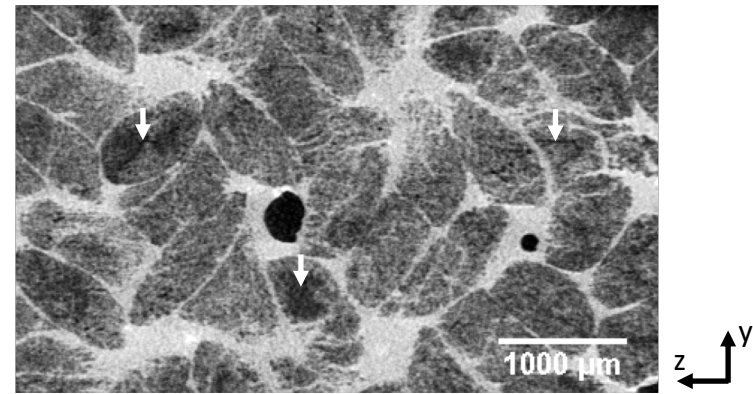
Figure 13: Maps of the evolution with increasing load of the average y -strain between the x - z planes at the upper and lower surfaces of (a) GSI and (b) PIP samples.



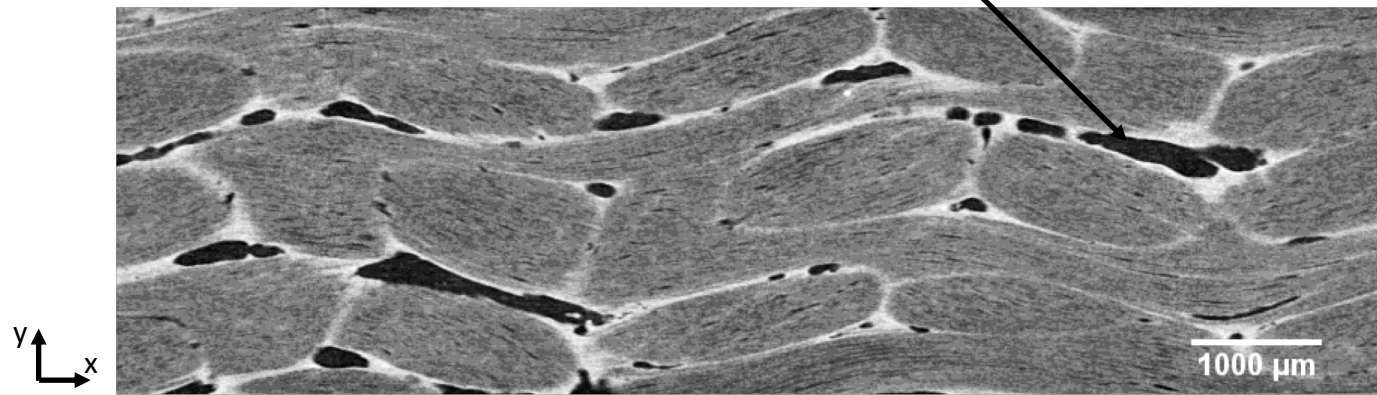


(a) (i) Initial intra-bundle crack

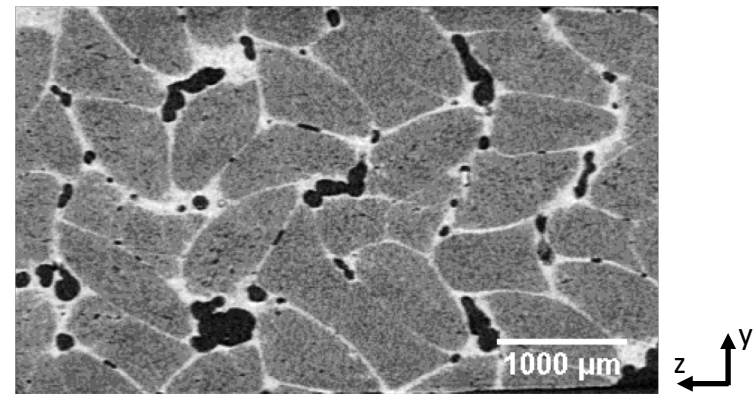
Inter-bundle pores



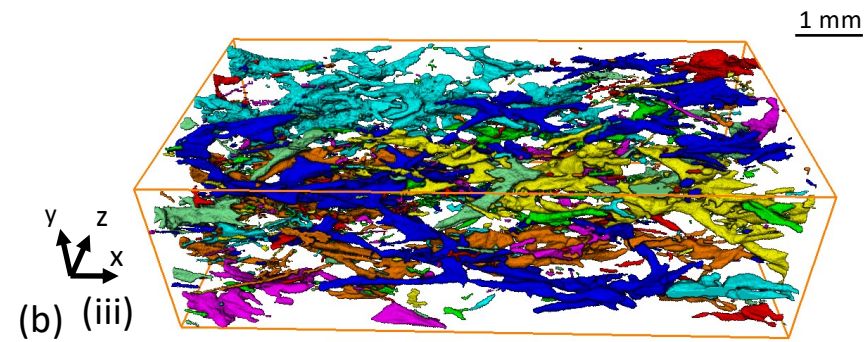
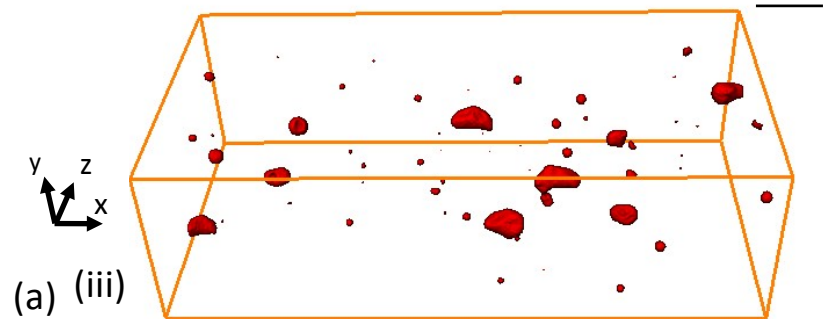
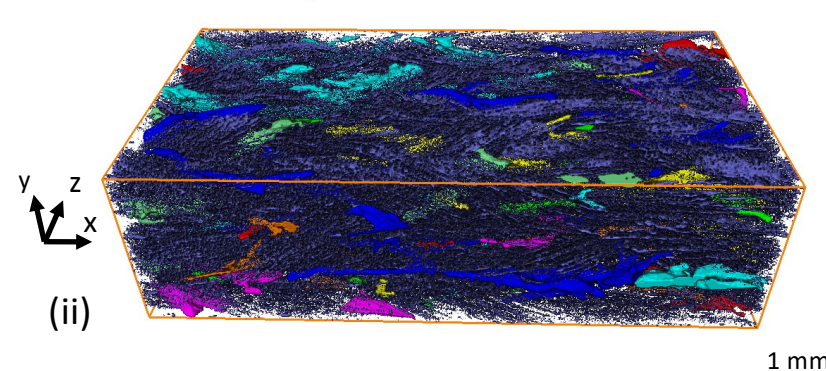
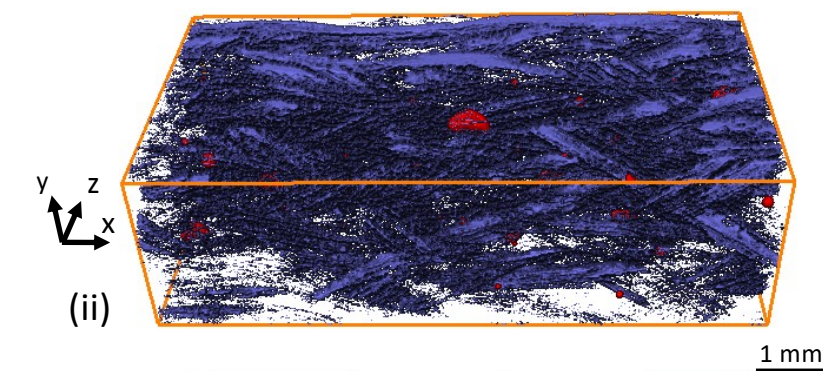
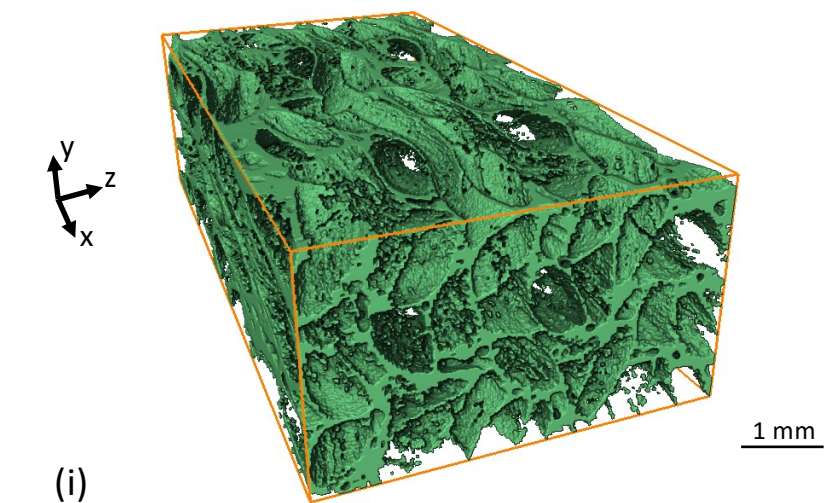
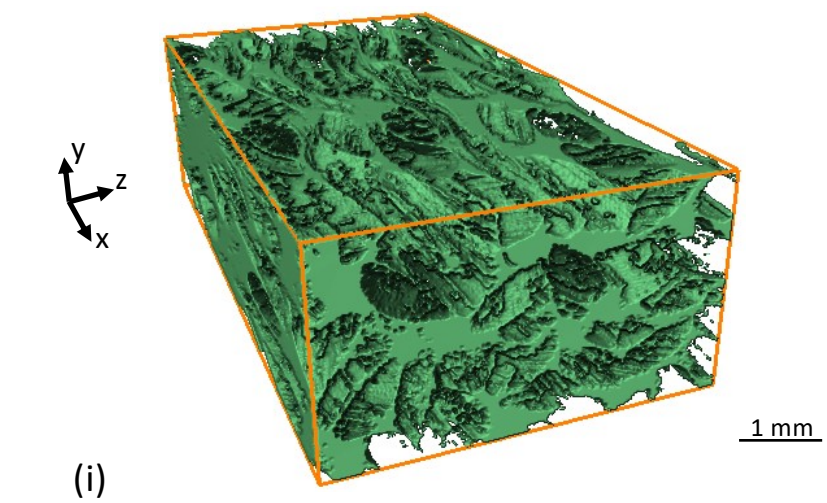
(ii)

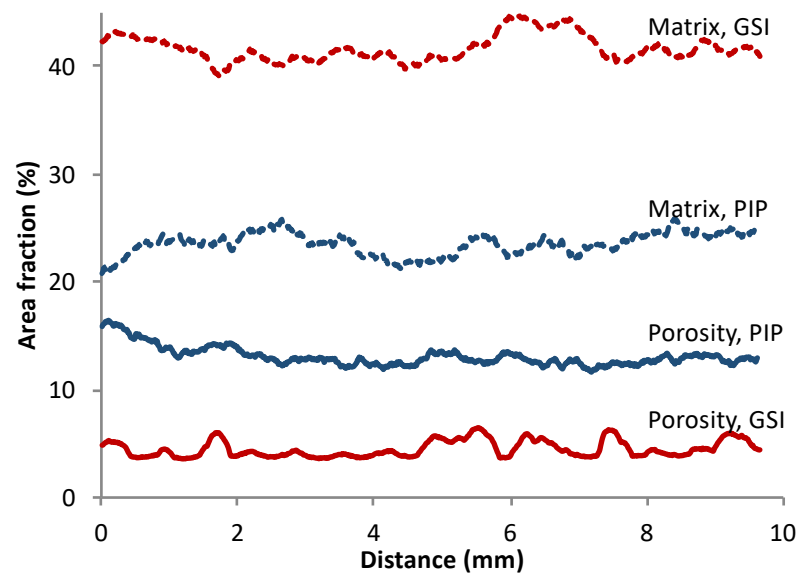


(b) (i)

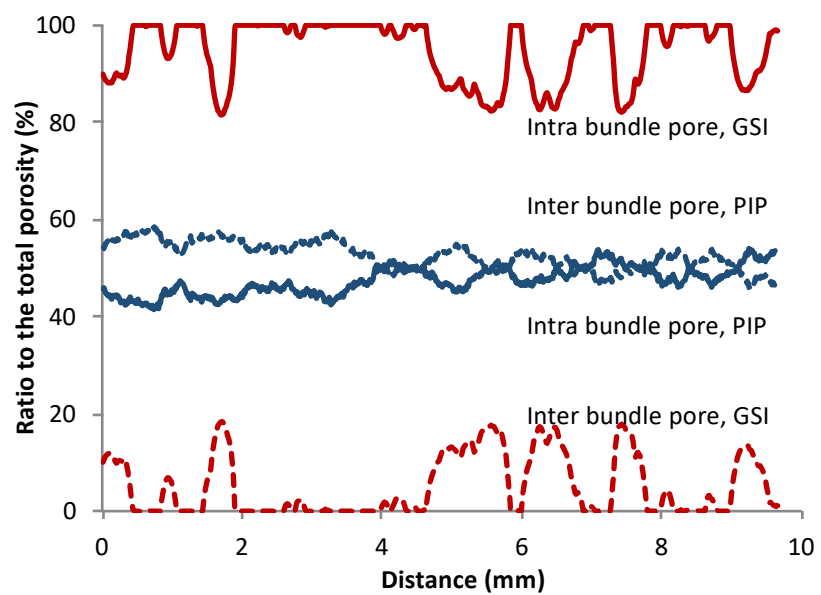


(ii)

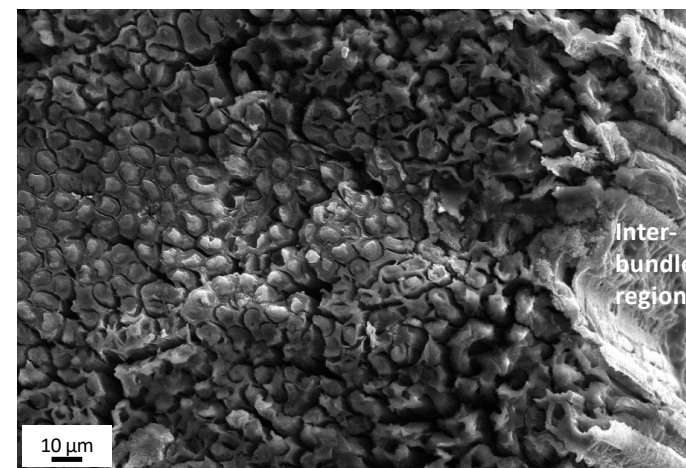




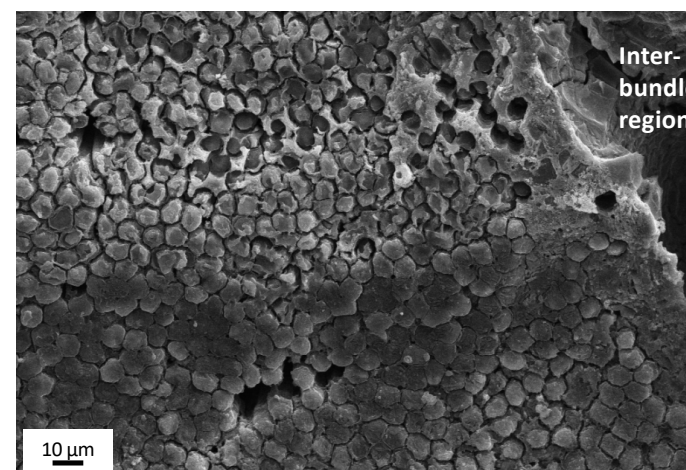
(a)



(b)

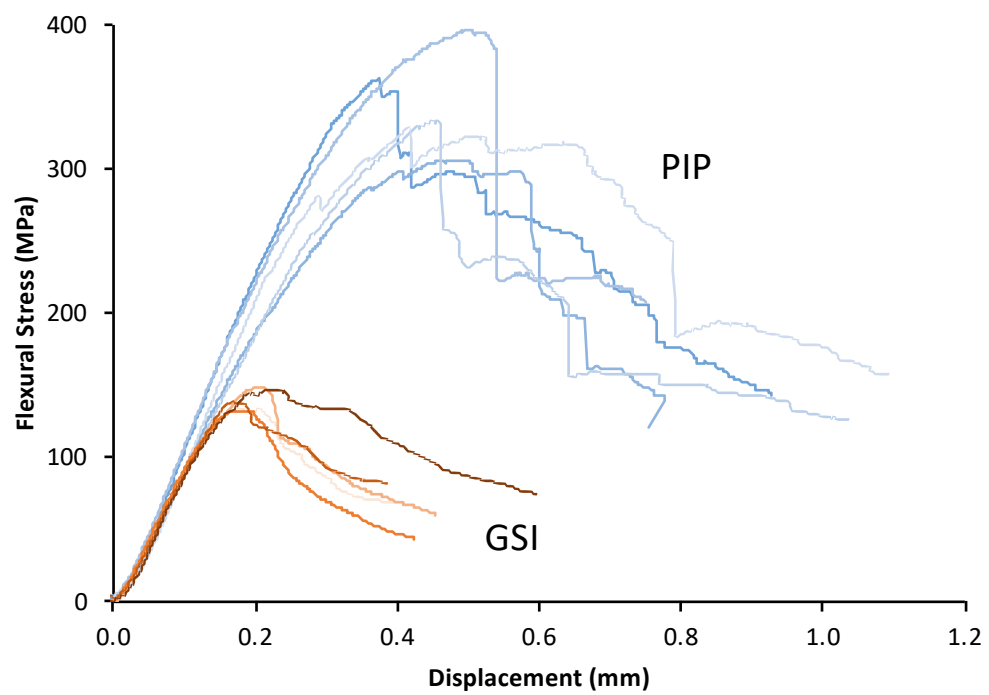


(i) GSI

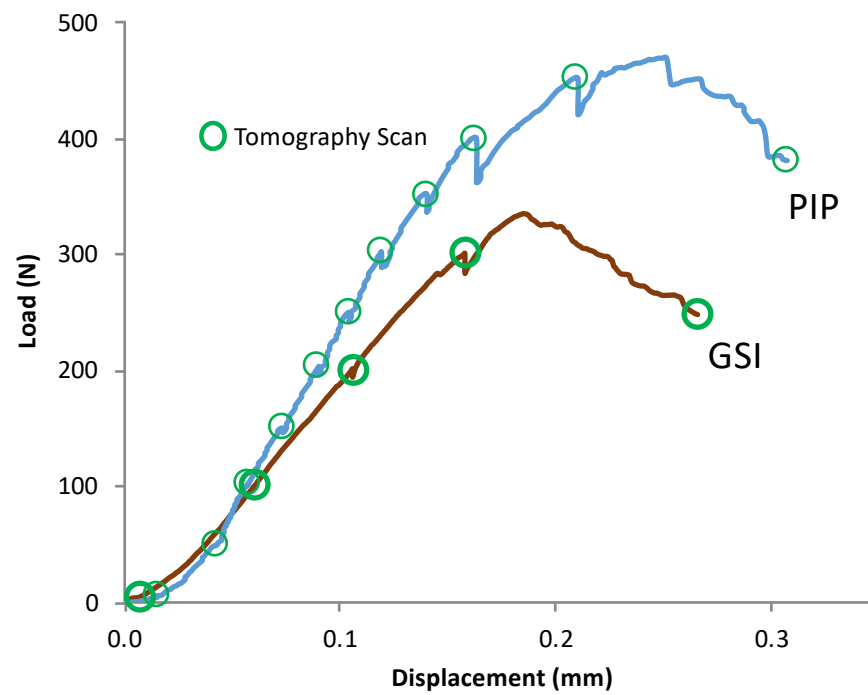


(ii) PIP

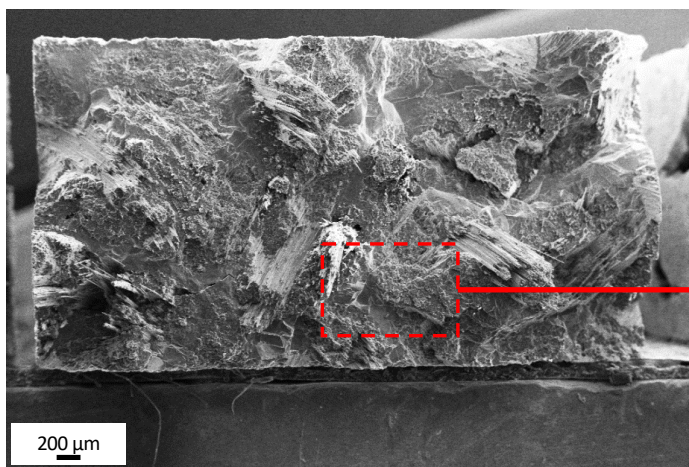
(c)



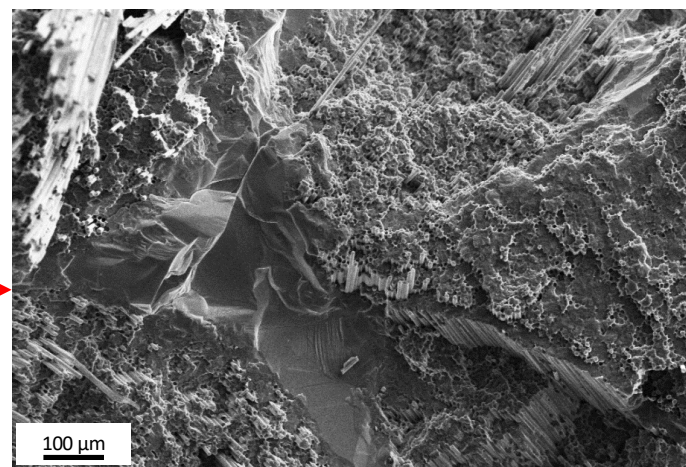
(a)



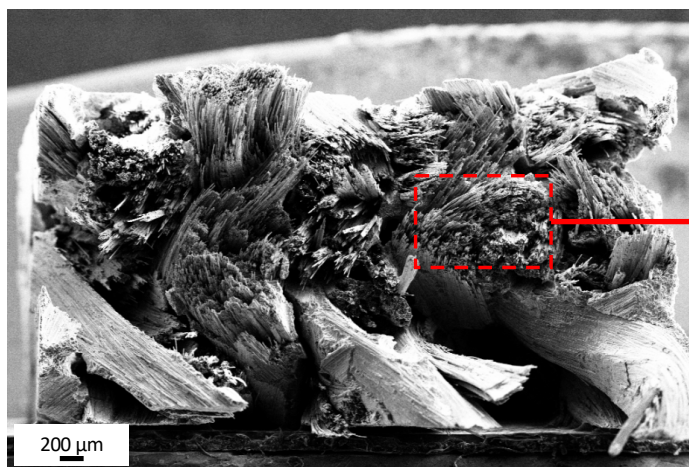
(b)



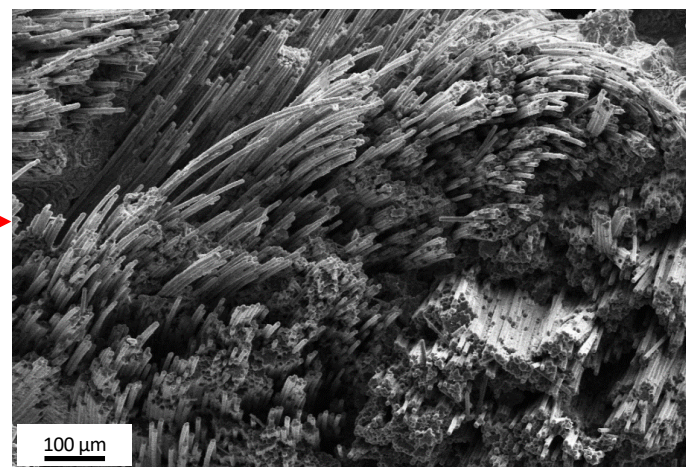
(i)
(a) GSI



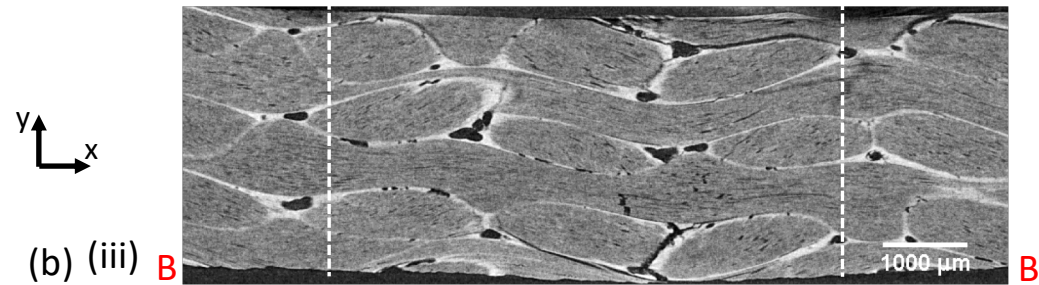
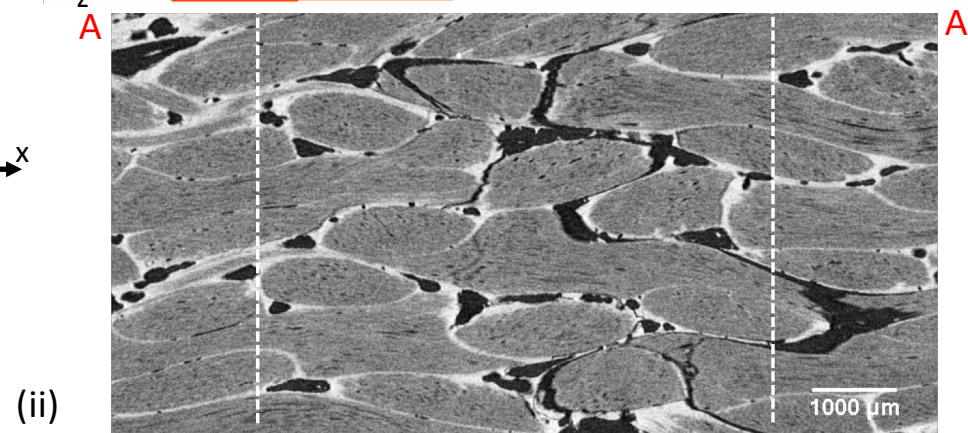
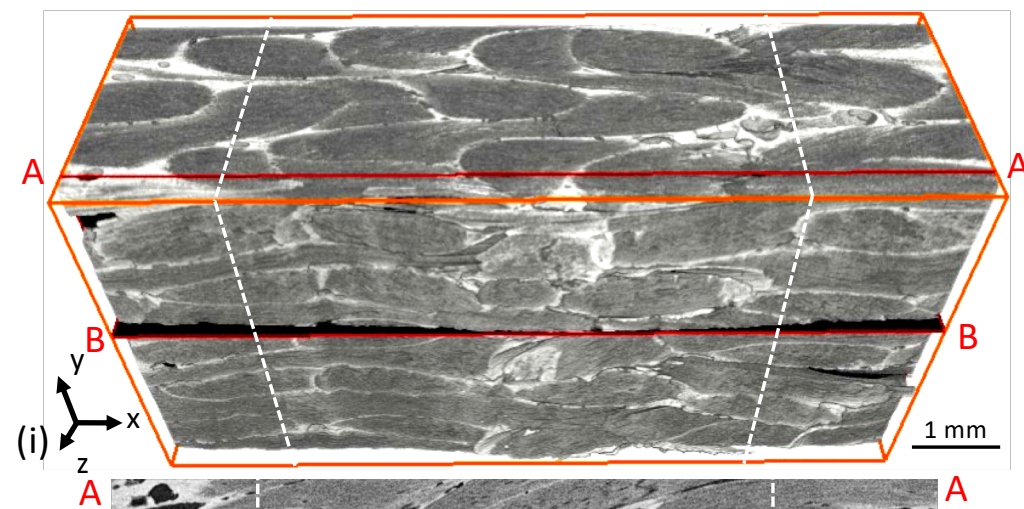
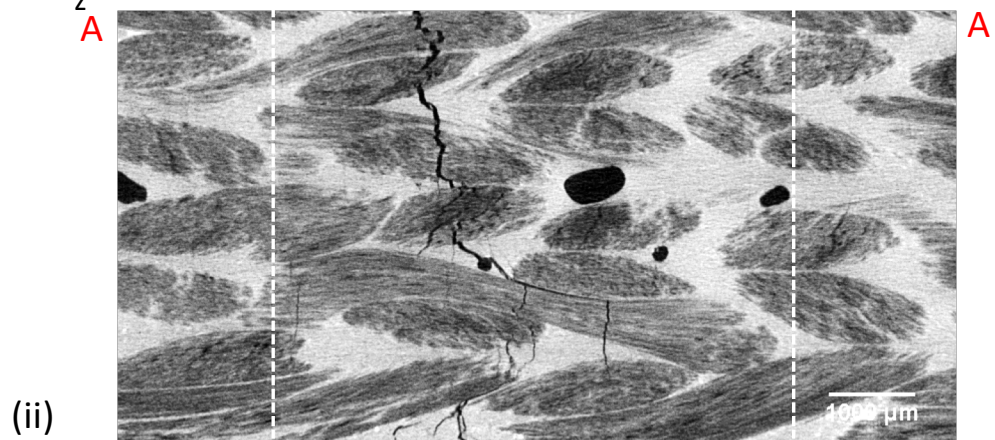
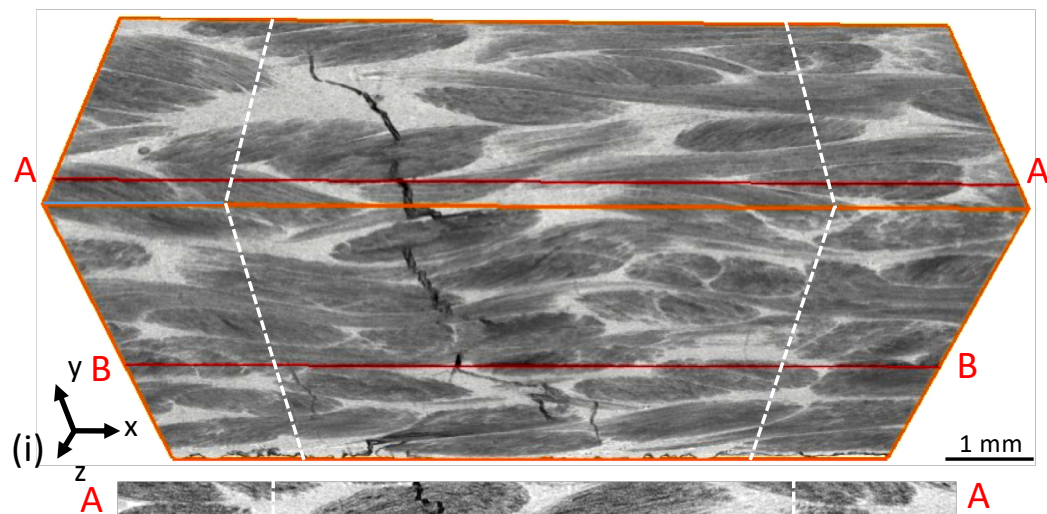
(ii)



(i)
(b) PIP

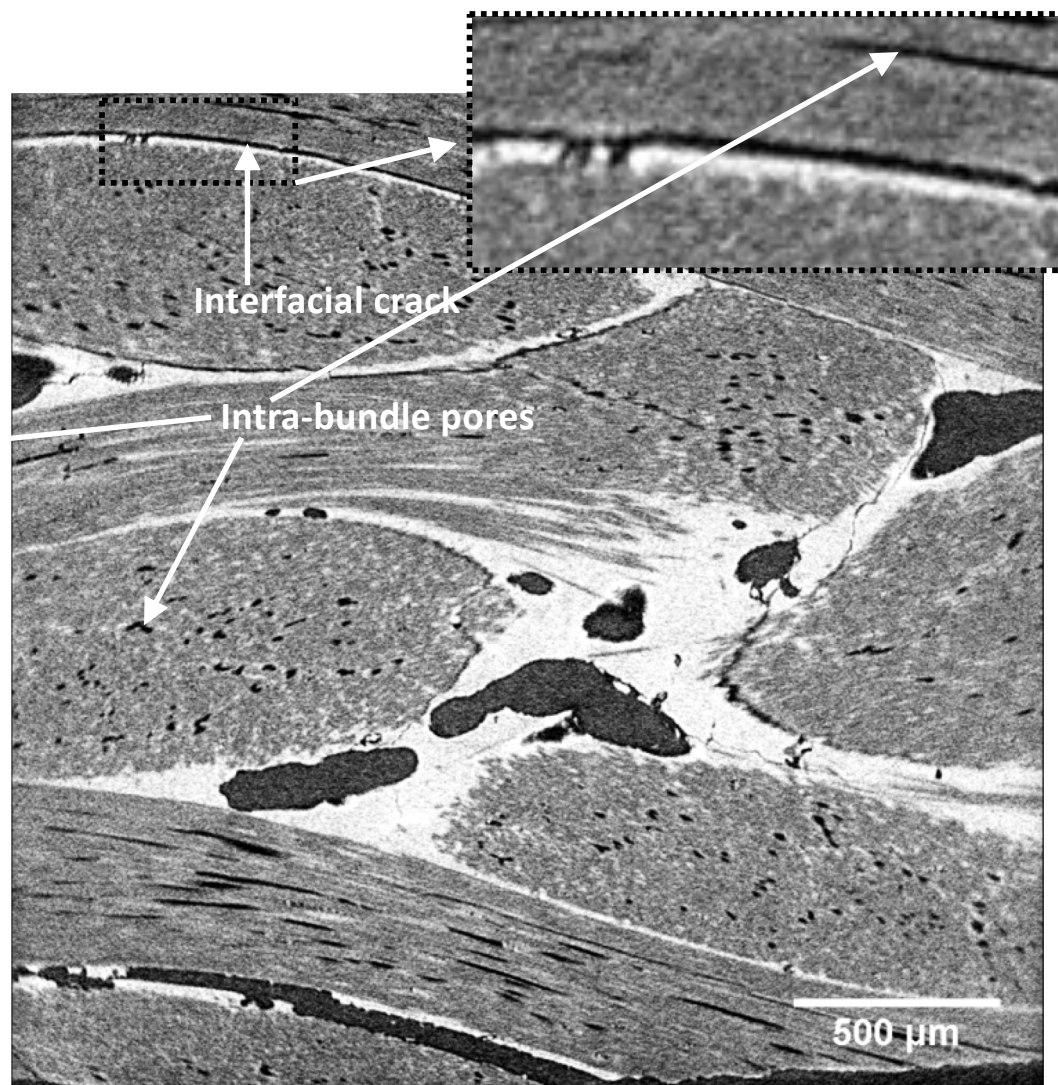


(ii)

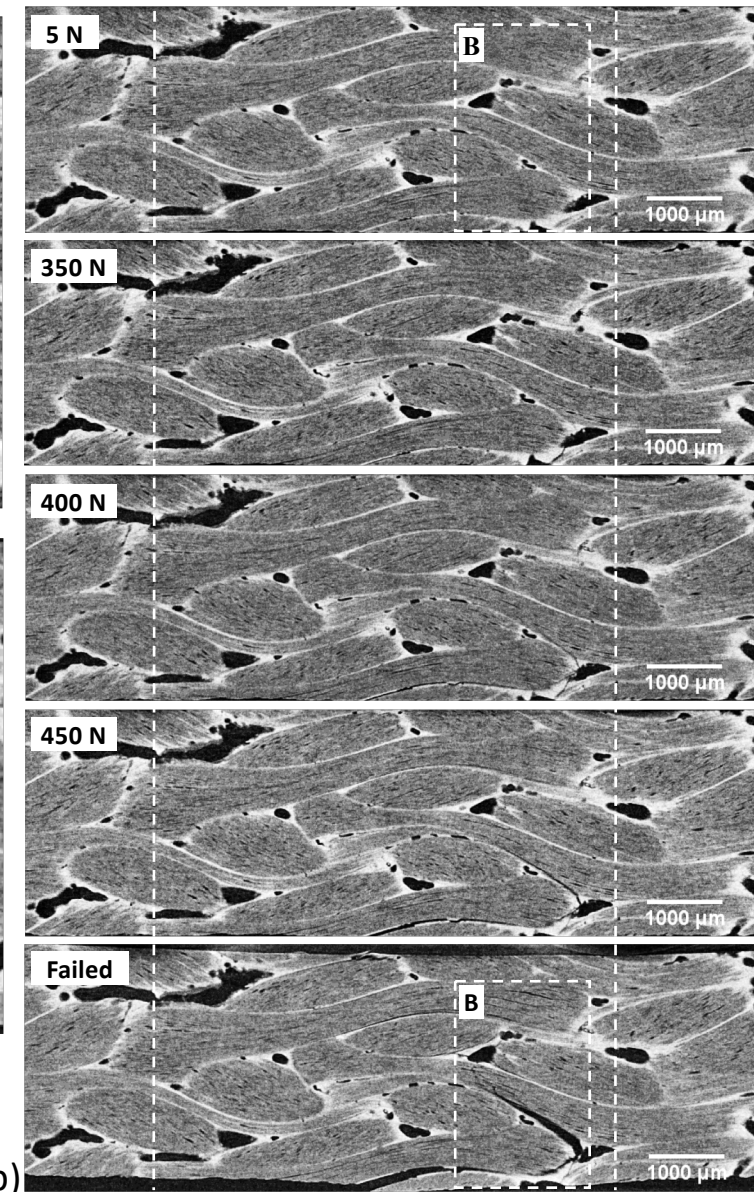
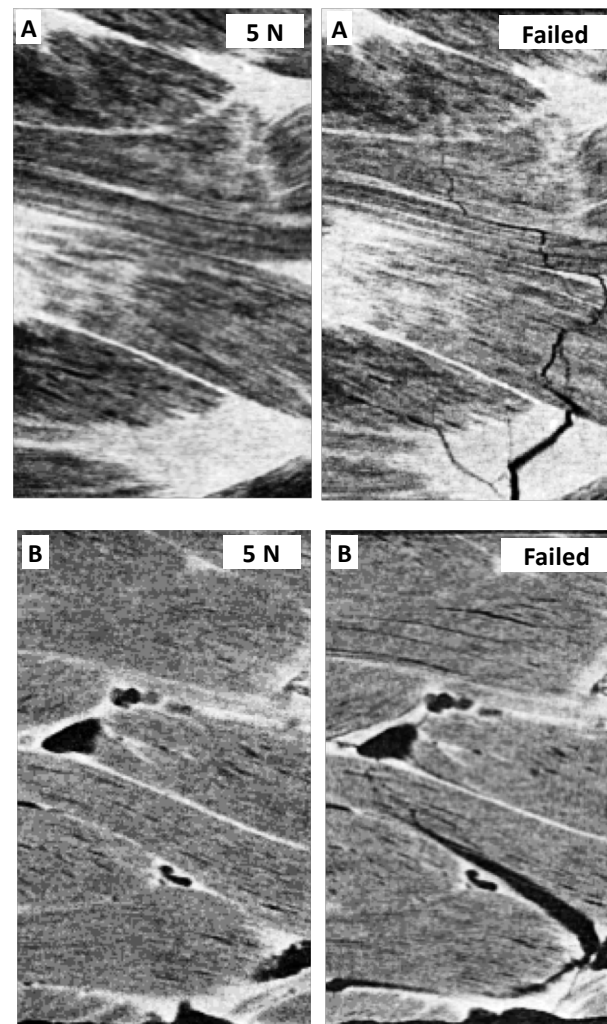
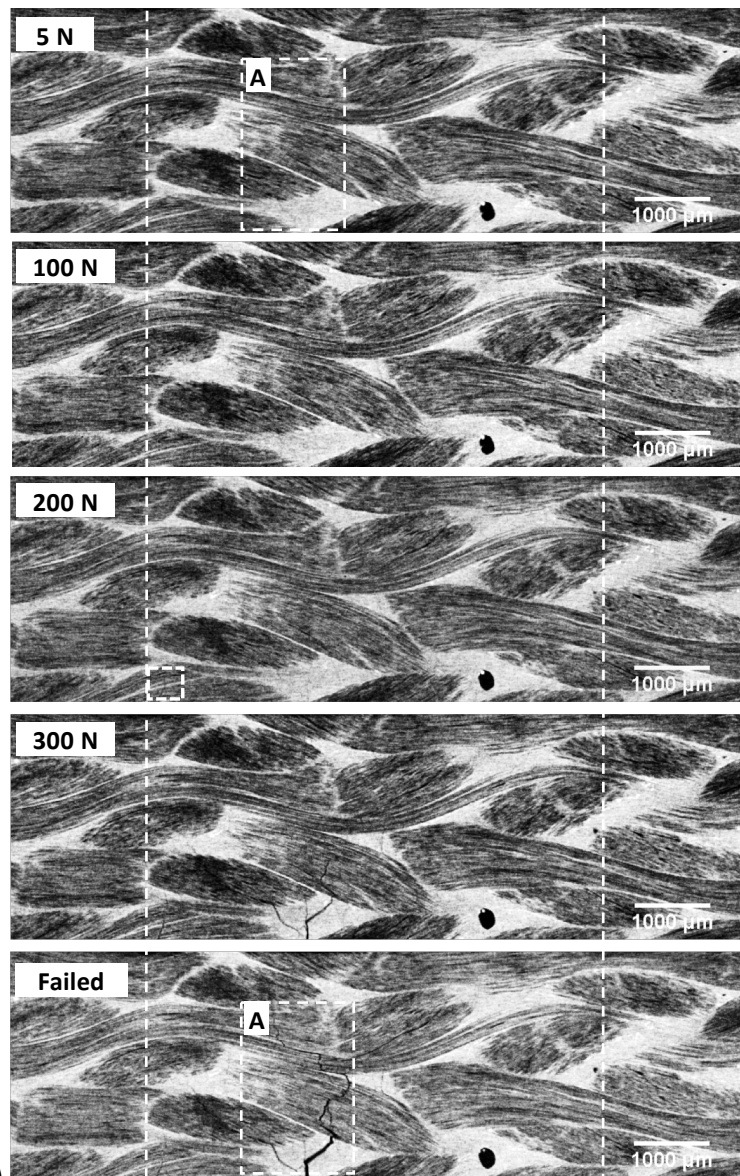




(a) $\begin{matrix} y \\ \uparrow \\ x \end{matrix}$



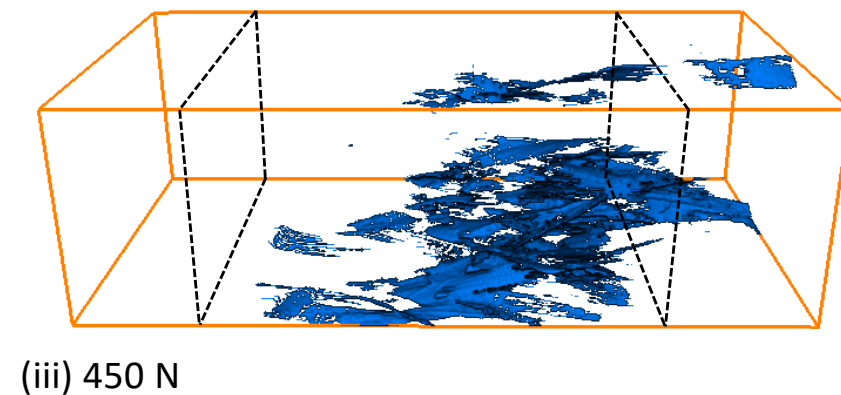
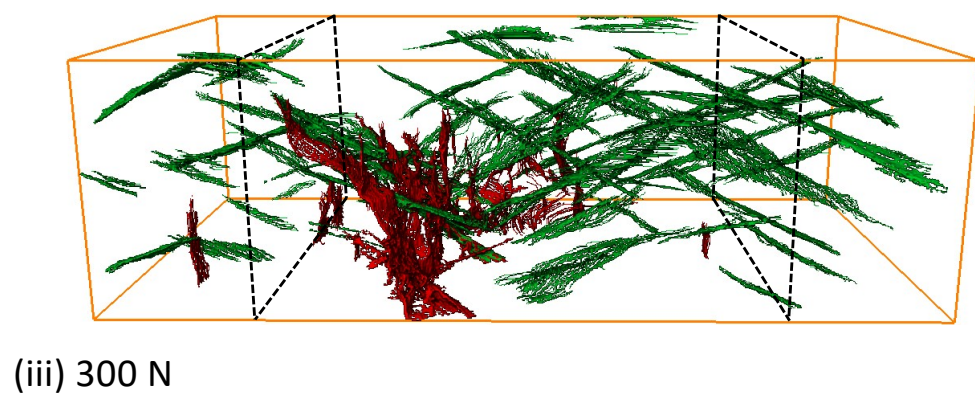
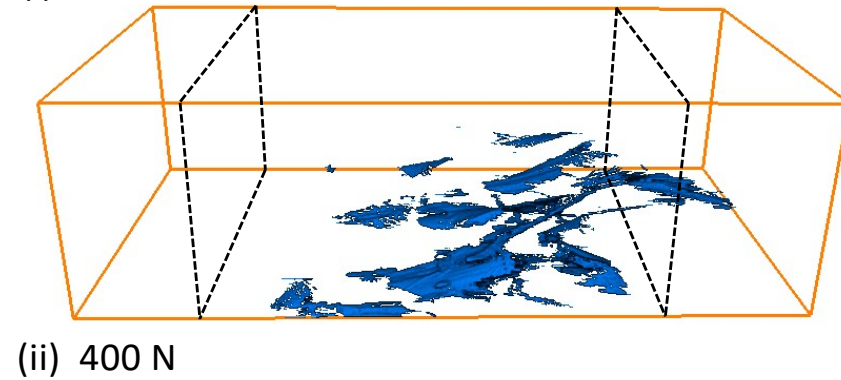
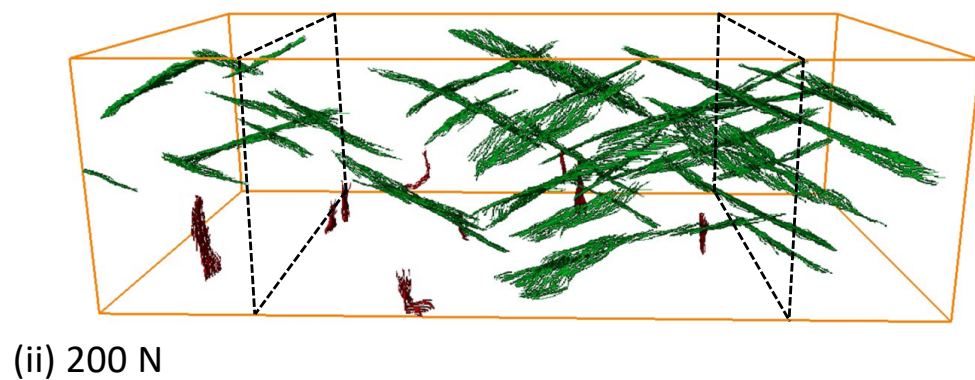
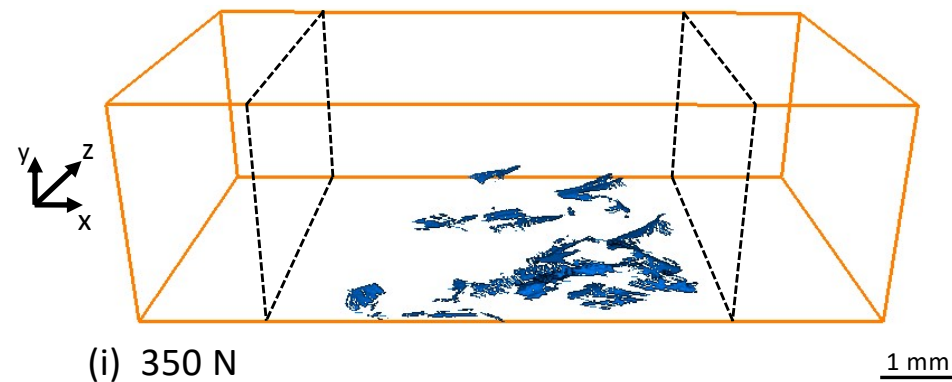
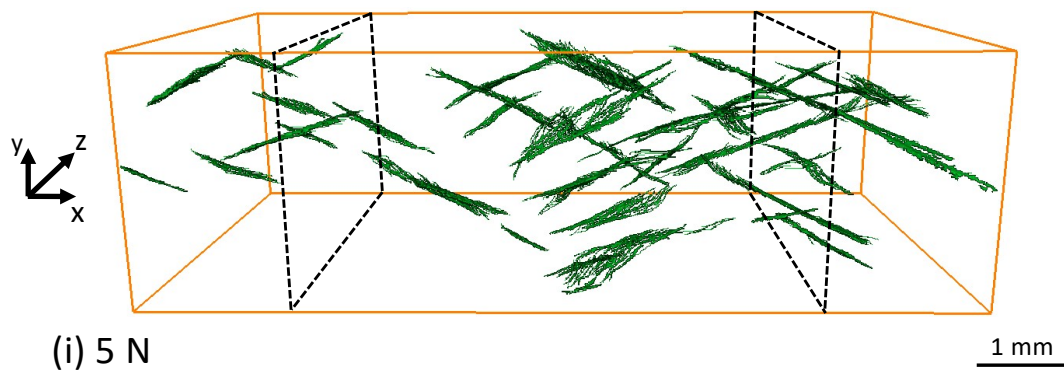
(b) $\begin{matrix} y \\ \uparrow \\ x \end{matrix}$

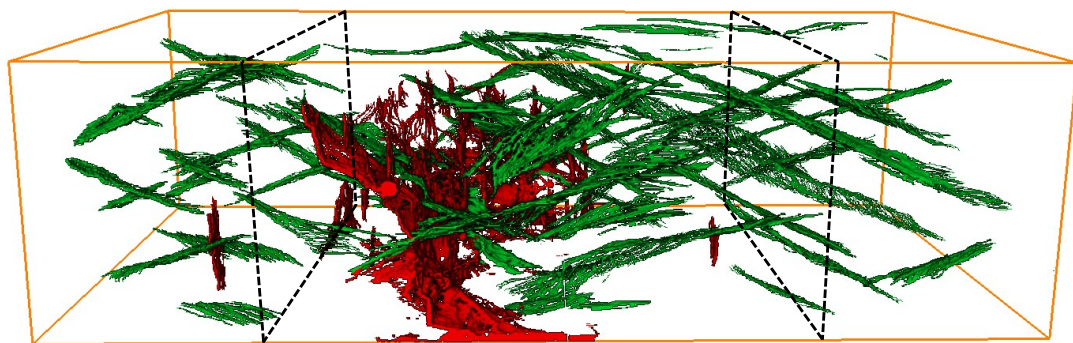


(a)

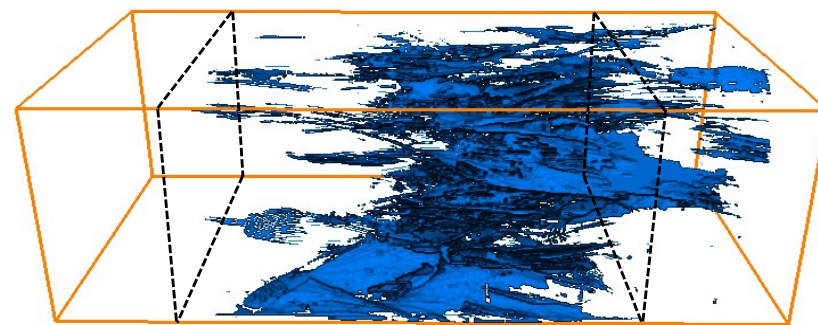
(b)

(c)

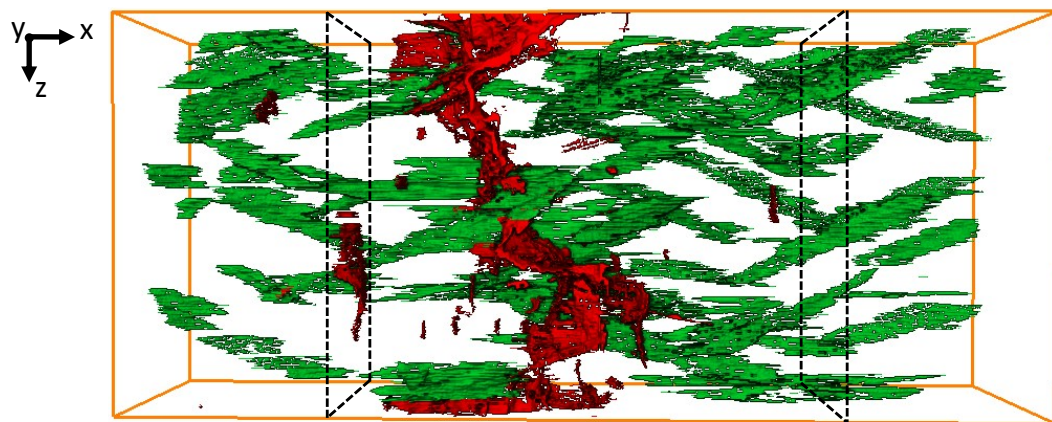




(iv) Failed

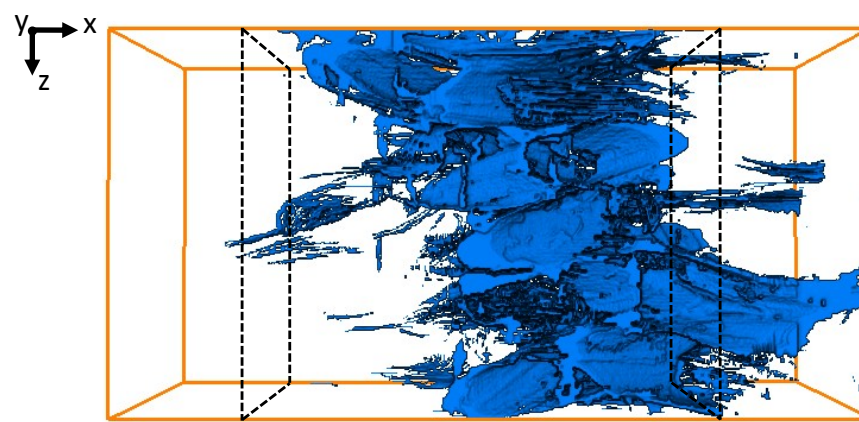


(iv) Failed



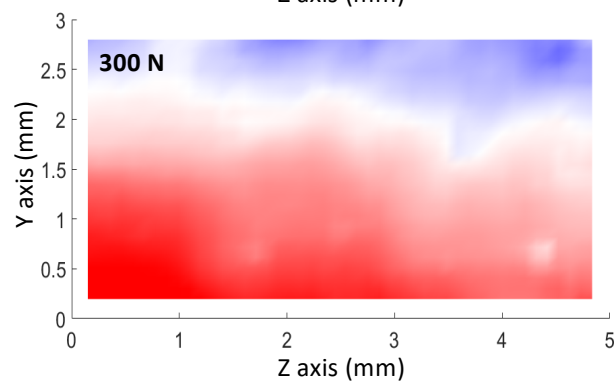
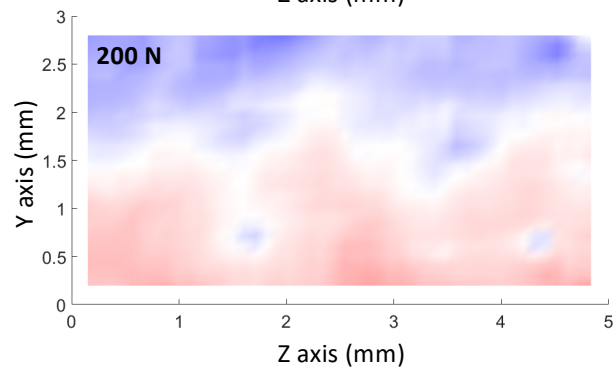
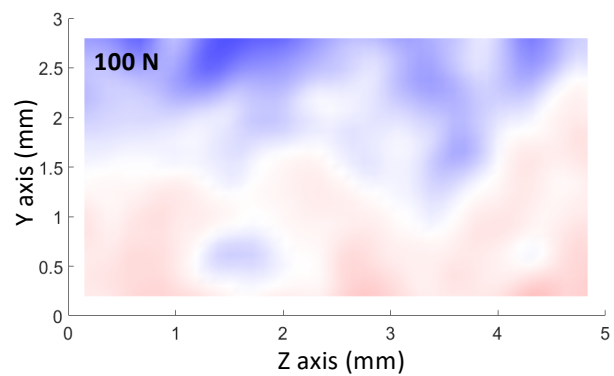
(v) Failed (bottom view)

(a)

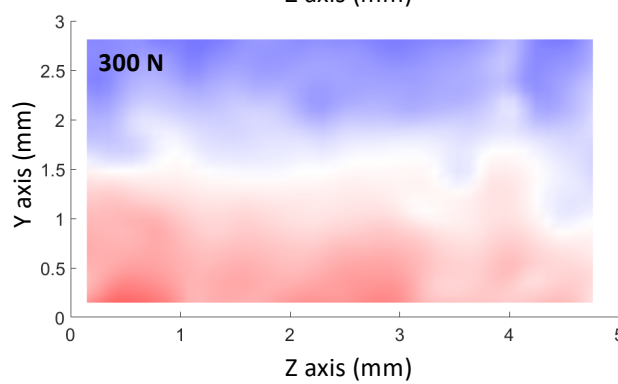
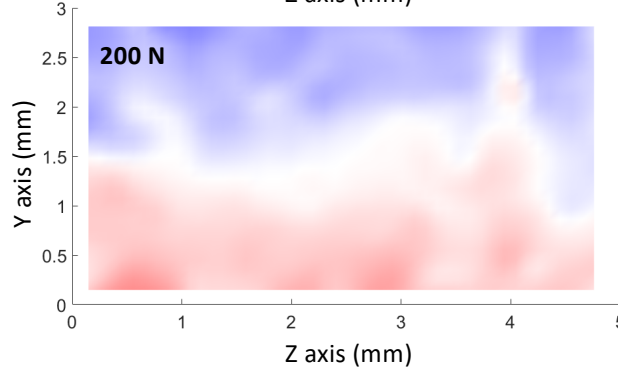
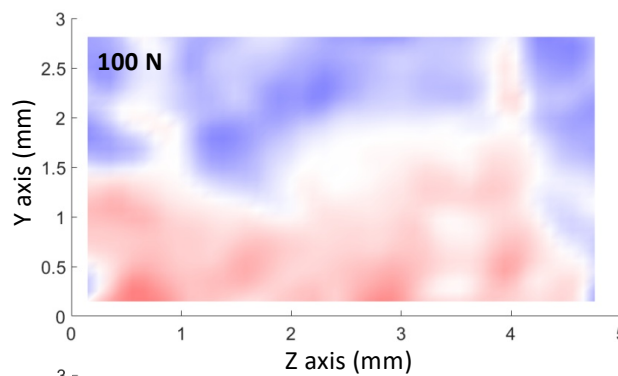


(v) Failed (bottom view)

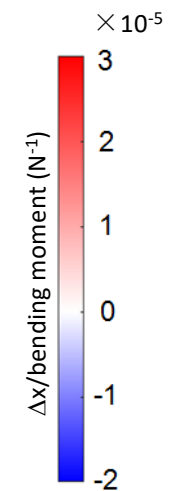
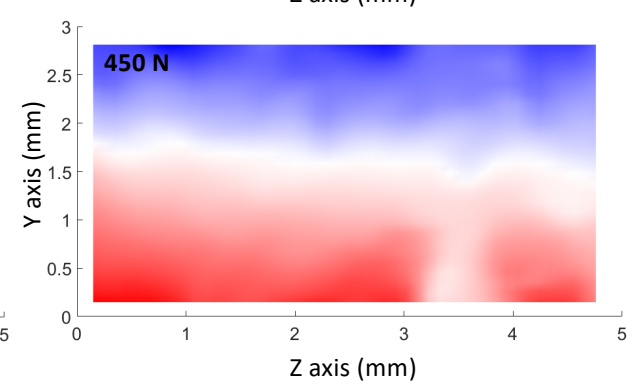
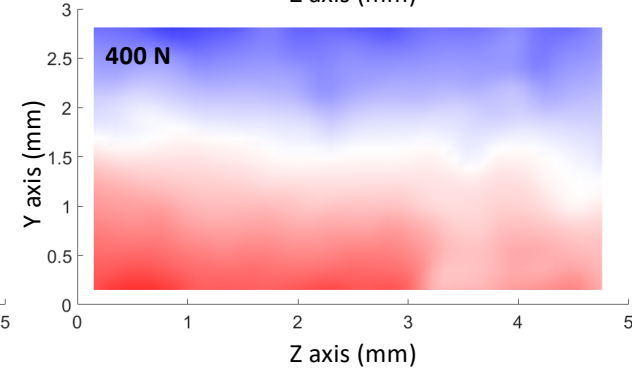
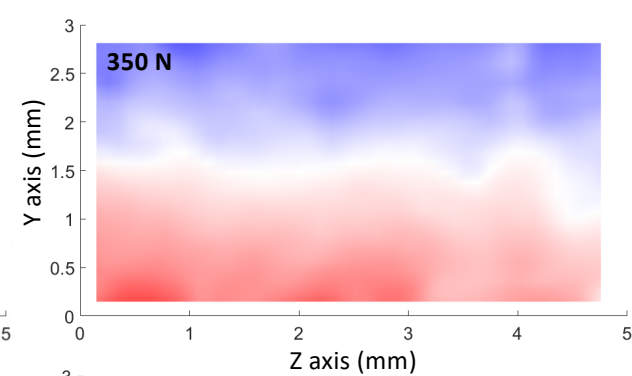
(b)

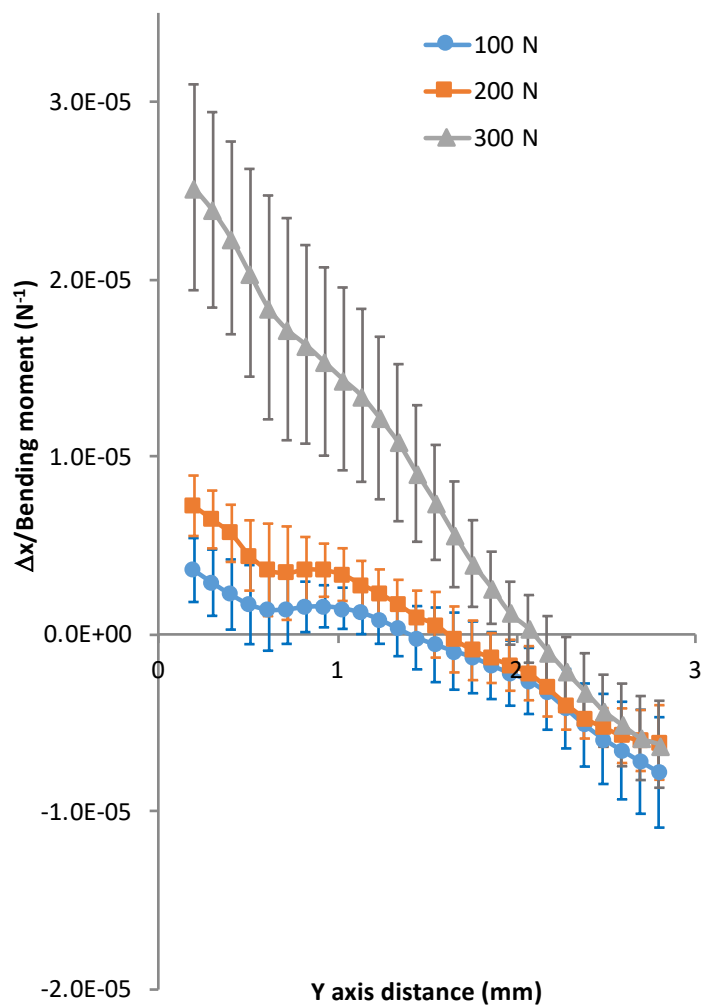


(a) GSI

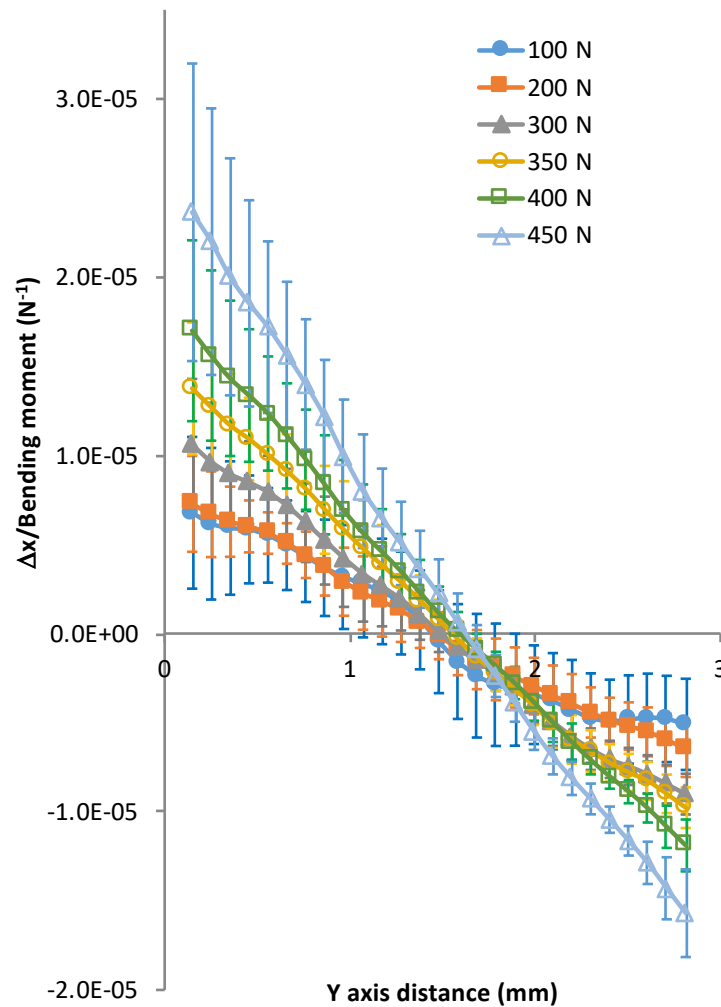


(b) PIP

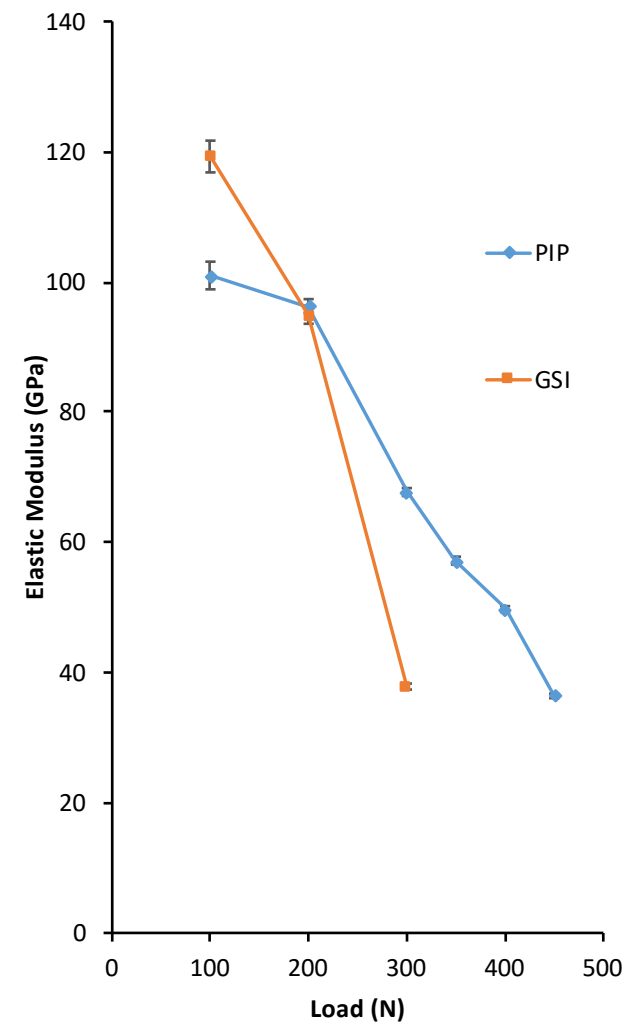




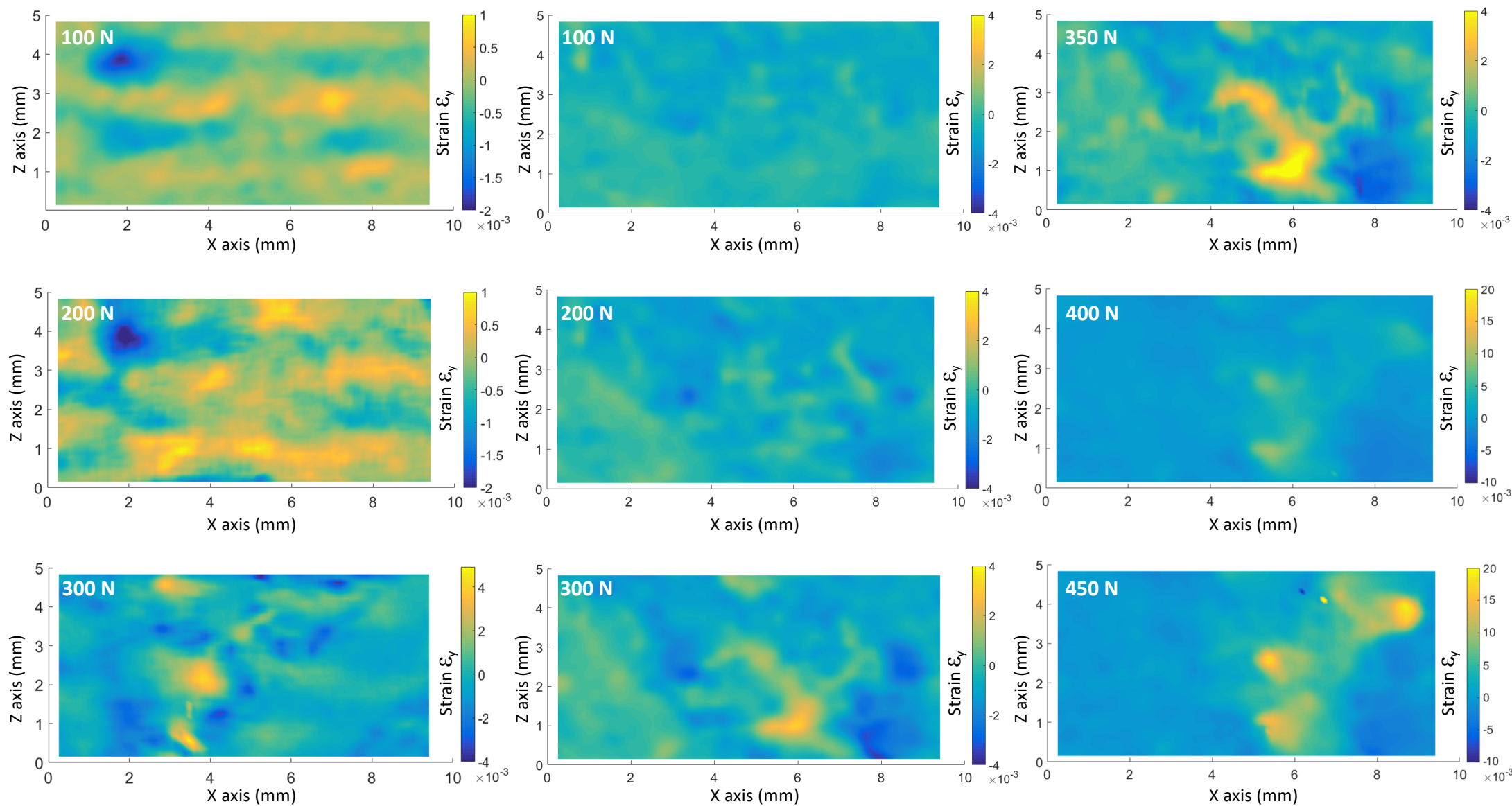
(a) GSI



(b) PIP



(c)



(a) GSI

(b) PIP